ELSEVIER

Contents lists available at ScienceDirect

Earth and Planetary Science Letters

journal homepage: www.elsevier.com/locate/epsl





Historic ocean acidification of Loch Sween revealed by correlative geochemical imaging and high-resolution boron isotope analysis of *Boreolithothamniom* cf. *soriferum*

Ellen MacDonald ^a, Gavin L. Foster ^{b,*}, Christopher D. Standish ^b, Jacob Trend ^b, Tessa M. Page ^b, Nicholas A. Kamenos ^{c,d}

- ^a School of Geographical and Earth Sciences, University of Glasgow, Glasgow, G12 8QQ, UK
- b School of Ocean and Earth Science, University of Southampton, National Oceanography Centre Southampton, Southampton, SO14 3ZH, UK
- ^c Department of Ecology and Environmental Science, Umeå University, Umeå, Sweden
- d Umeå Marine Sciences Centre, Umeå University, Norrbyn, Sweden

ARTICLE INFO

Editor: Bao

Keywords: Coralline algae Boron isotopes Ocean acidification Correlative imaging

ABSTRACT

Ocean Acidification (OA) arises from the increase in atmospheric carbon dioxide concentration following the industrial revolution. The ecological and socio-economic consequences of OA were first identified around 10-15 years ago but remain poorly understood. This is particularly true in coastal regions where local processes can have dramatic consequences on pH trends through time, obscuring and compounding the long-term effects from rising atmospheric CO2. Here we explore the possibility of generating long records of coastal ocean pH using the skeletons of widely distributed coralline algae (CA). The skeletons of these slow growing (<1 mm/year) taxa often contain micron-scale heterogeneities, making sampling for high-resolution climate reconstructions using bulk sampling techniques difficult. Here we use laser ablation coupled to inductively coupled plasma mass spectrometers to generate high-resolution 2D images of the element/calcium ratios and boron isotope composition (δ^{11} B) of a sample of Boreolithothamniom cf. soriferum from Loch Sween in Scotland, UK where we have been monitoring temperature since 2004 and pH during 2014. By carefully correlating the geochemical images with a scanning electron microscopy image we can segment them to remove the marginal portions of the skeleton, isolating the central growth axis to generate an age model and growth rate. The δ^{11} B-pH is significantly elevated above the seawater pH in Loch Sween (8.4 to 8.9 vs. 7.9 to 8.1) consistent with other CA that show internal pH elevation. On a seasonal scale, internal pH is negatively correlated with temperature and also exhibits a long-term decline. By removing this temperature effect, internal pH can be correlated to seawater pH during the 2014 monitoring period allowing us to reconstruct a seawater acidification trend from 2004 to 2018 of -0.018 pH units per year, 10x higher than open ocean trends but consistent with contemporaneous monitoring efforts of UK coastal waters. Reconstructed aqueous CO₂ suggests that prior to ~2008 Loch Sween was a sink of CO2 but after this date, particularly during the early summer, it was a substantial CO2 source. Comparison of reconstructed aqueous CO2 with a record of calcification rate of our sample of Boreolithothamniom cf. soriferum suggests this acidification and associated rise in local seawater pCO2 may have freed this sample from carbon limitation leading to a recent increase in calcification.

1. Introduction

The ocean has absorbed around 25% of the CO_2 released to the atmosphere since the industrial revolution. Ocean acidification, the unavoidable consequence of that CO_2 uptake, is the result of the simultaneous changes in the concentrations of H^+ , CO_2 , bicarbonate

(HCO $_3$) and carbonate (CO $_3^2$) following the dissociation of carbonic acid (H $_2$ CO $_3$) in seawater. Since the start of the industrial revolution in ca. CE 1850, globally averaged surface water pH (-log $_{10}$ [H $^+$]) has declined by ca. 0.1 pH units (a 25% increase in H $^+$ ion concentration) while CO $_3^2$ has declined by \sim 20%. Depending on emission scenario, the magnitude of OA could reach as much as 0.4 pH units by 2100 (Gattuso et al., 2015).

E-mail address: g.l.foster@soton.ac.uk (G.L. Foster).

^{*} Corresponding author.

Although organisms producing calcium carbonate shells, tests and skeletons experience the strongest negative effects from ocean acidification (e.g. Gattuso et al., 2015), the impacts are felt across marine ecosystems (e.g. Ferrari et al., 2012). Likely negative effects include (but are not limited to): increased mortality of shelled organisms (e.g. White et al., 2014), increased chemical erosion of reef structures such as coral reefs (e.g. Eyre et al., 2018), and shifts in species composition away from calcifiers (e.g. Brodie et al., 2014). The projected costs of ocean acidification on the ecosystem services provided globally by coral reefs, wild fisheries, and aquaculture is estimated to be in excess of \$1 trillion (Secretariat of the Convention on Biological Diversity, 2014).

While the magnitude of open ocean trends in pH are relatively welldocumented and understood (e.g. Bates et al., 2014), pH variability on daily to decadal timescales in nearshore and coastal environments is very large (i.e. $>\pm$ 0.4 pH units; e.g. Carstensen and Duarte, 2019; Duarte et al., 2013). This is the result of local hydrodynamic (e.g. mixing/stratification, local currents, freshwater inflows) and biological processes (e.g. ecosystem primary productivity, respiration and calcification) that can drive dramatic changes in dissolved inorganic carbon (DIC) and total alkalinity (ALK), and thereby, pH (Carstensen and Duarte, 2019). This confounds attempts to accurately determine the full magnitude of past and future ocean acidification in these regions (Sutton et al., 2019), a difficulty that is further compounded by the relatively short interval covered by the available high quality carbonate chemistry records in these environments (i.e. <10 years in most cases). While there are considerable efforts to establish coastal carbonate system monitoring networks, natural variability is so large that the emergence of long-term trends will require >25 years of monitoring (e.g. Sutton et al., 2019). There is therefore an urgent need to better understand the natural and anthropogenic trends of pH in coastal regions, particularly given that pH change in these regions is likely to have the largest impact on humanity (Fitzer et al., 2014). However, continuous and reliable time series of pH in coastal waters prior to around the early 2000s are sparse and entirely lacking for many regions of the globe. One way to gain a long-term view of coastal ocean pH is to reconstruct it from the boron isotopic composition of marine calcifiers (e.g. D'Olivo et al. 2019; Fietzke et al., 2015). Scleractinian coral skeletons are particularly useful in this regard (D'Olivo et al., 2019) because they have an annually banded skeleton, relatively high annual growth rates (up to 20 mm yr⁻¹) and high boron concentrations, allowing monthly resolved records of past coastal pH to be constructed. Scleractinian corals, however, are only found in the tropical ocean and therefore we must look to other archives to get a global picture of the evolution of coastal pH.

One such archive that is receiving increasing attention is the high-Mg calcite skeletons of coralline algae (CA). CA have a near global distribution in coastal waters (van de Heijden and Kamenos, 2015) where they are key ecosystem engineers, and also form annually banded skeletons like corals. However, unlike corals where calcification occurs largely within an isolated space between the coral animal and the existing skeleton (Gilbert et al. 2022), CA calcification occurs within the outer cell walls of the epithelial cells that cover the outer surface of the skeleton (Nash et al., 2019). Previous work using boron isotopes (expressed as δ^{11} B) has shown that the pH of the fluid from which calcification occurs in CA is significantly higher than seawater (Fietzke et al., 2015; Cornwall et al., 2017; Donald et al., 2017; Anagnostou et al., 2019; Fig. 1), although for CA the exact processes responsible for this observation remain the subject of discussion (e.g. Nash et al., 2019; Cornwall et al., 2017; McCoy et al., 2023). Regardless, internal

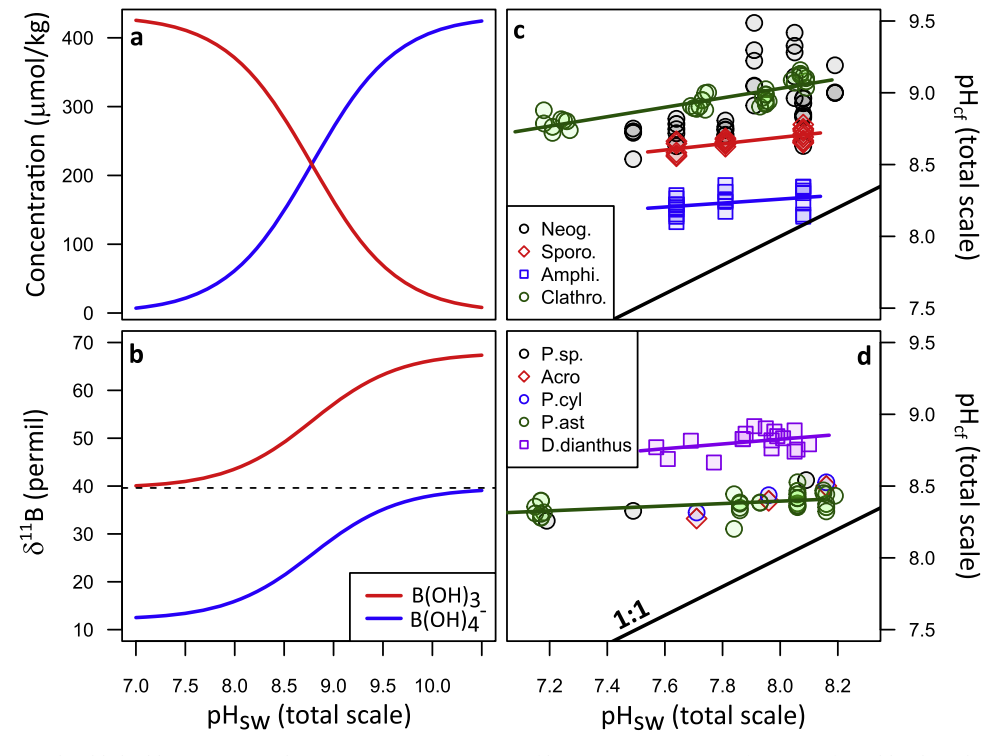


Fig. 1. Boron systematics and published boron isotope data. (a) aqueous speciation of boron in seawater as a function of pH, blue line shows the concentration (in μ mol kg⁻¹) of borate ion and red line shows the concentration of boric acid. (b) boron isotopic composition (as δ^{11} B in permil) for both aqueous species as a function of pH. The dotted line is the boron isotopic composition of total boron in seawater (39.61 %; Foster et al., 2010). Calculated with the seacarb package in R (Gattuso et al., 2022) with a temperature = 10 °C and salinity of 35 for illustrative purposes. (c) Published δ^{11} B data for coralline algae. *Sporolithon durum* (Sporo.), *Amphiroa anceps* (Amphi) and some of the *Neogoniolithon* sp. (Neog.) data from Cornwall et al. (2017) with the remaining *Neogoniolithon* sp. data from Donald et al. (2017). *Clathromorphum compactum* (Clathro.) data from Anagnostou et al. (2019). (d) A selection of the published δ^{11} B data for scleractinian corals. *Porites* sp. (P.sp.) are from Krief et al. (2010), *Acropora noblis* (Acro) and *Porities cylindrica* (P.cyl) data are from Hönisch et al. (2004), *Porites asteroides* (P.ast) data are from Eagle et al. (2022), *Desmophyllum dianthus* (D. dianthus) data are from Rae et al. (2018) who supplemented the dataset of Stewart et al. (2016). Ordinary least squares best fit lines in (c) and (d) were drawn using R.

calcification pH in CA has been shown to vary as a function of external pH, albeit 1 pH unit of external pH change is typically associated with <0.5 pH units of internal pH change (Fig. 1). Mg/Ca ratios in CA skeletons have been used for some time to reconstruct coastal temperatures (e.g. Halfar et al. 2000; Kamenos et al., 2012) and more recently Fietzke et al. (2015) used an innovative laser ablation approach to measure the δ¹¹B of the skeleton of Clathromorphum nereostratum, documenting a trend of increasing ocean acidification through the 20th century at Attu Island, Alaska. In situ techniques like laser ablation are particularly well-suited for analysis of CA because some species are comparatively slow growing (< 1 mm yr⁻¹), particularly at high latitudes where growth rates can be as low as 100 µm yr⁻¹ (Kamenos and Law, 2010). Furthermore, there is considerable heterogeneity at the micron-scale in many species of CA and laser ablation and other in situ sampling techniques such as electron microprobe analysis allow the primary high-Mg calcite to be targeted (Halfar et al., 2000). These heterogeneities are associated with reproductive structures known as conceptacles which are cavities that can form annually through dissolution of existing skeletal material (Adey, 1965) and are often infilled with secondary phases (e.g. dolomite). The skeletal material around the conceptacles is also frequently morphologically and chemically distinct (Fietzke et al., 2015).

Several studies have generated 2D geochemical maps of CA skeletons, elegantly overcoming many of these sampling issues (e.g. Halfar et al. 2000; Fietzke et al., 2015). However, correlative multimodal imaging (CMI; Karreman et al., 2016; Walter et al., 2020; Zopf et al., 2021; Standish et al., 2024), where images from different methods and of different resolution are precisely combined to generate a holistic view of a sample, is rarely carried out. Indeed, CMI is not often applied in the Earth and Environmental Sciences, despite its use in other fields and its potential utility in the study of material like CA skeletons. Here we apply a range of techniques (scanning electron microscopy, laser ablation inductively coupled plasma mass spectrometry (LA-ICPMS)) to image the structure, element/calcium (E/Ca) and boron isotopic composition of a sample of Boreolithothamniom cf. soriferum, hereinafter referred to as B. soriferum, from Loch Sween in Scotland UK. By precisely correlating the different imaging modalities we not only gain valuable insights into the environmental sensitivity of calcification in this species of CA, but we are also able to reconstruct ocean acidification trends in Loch Sween over the last 20 years which compare favourably with nearby data from the UK ocean pH monitoring network (e.g. Ostle et al., 2016; Findlay et al., 2022).

2. Methods

2.1. Sample description, location and imaging

Live thalli (rhodoliths) of *B. soriferum* CS9 were collected at 5 m depth by SCUBA from a coralline algae bed in Loch Sween, Scotland (56°01.99′N 05°36.13′W; Fig. S1). This species was initially identified as *Lithothamnion glaciale* at this site using traditional taxonomy (Irvine and Chamberlain, 1994) and then *Lithothamion soriferium* using barcoding (Peña et al. 2021). Subsequent advances in sequencing have enabled more taxonomic resolution and this species has now been re-classified as *Boreolithothamnion soriferum* (Gabrielson et al., 2023).

Loch Sween is fully marine sea-loch, with algae bed temperature range of 6–17 $^{\circ}$ C and average pH of 8.10 (Attard et al., 2015). The sample was transported to the School of Geographical and Earth Sciences, University of Glasgow, to be dried and individual branches mounted in Buehler EpoThin resin. These were then polished to form transverse section and BSE images were collected on a Carl Zeiss Leo 1450VP scanning electron microscope (SEM) with W filament at the University of Southampton before and after laser ablation. Unlike many species of coralline algae, *B. soriferum* from this location rarely contains conceptacles (Kamenos and Law, 2010). Prior to ablation the sample was cleaned in a solution of 1% H₂O₂ and 0.1 M NH₄OH for 20 h before being ultrasonicated for 5 min and rinsed three times in 18.2 M Ω cm

(ultrapure) water to remove surficial organic material.

Instrumental pH data from Loch Sween were sourced from Mao (2019). A YSI EXO2 sonde was deployed in the same rhodolith bed to record pH for the period 14/08/13 to 25/07/14 (15-minute interval sampling). During the deployment the instrument was calibrated monthly using manufacturers specifications, with pH calibrated on the NBS scale and converted to pH Total scale following Peltzer (1998).

2.2. Boron isotope measurements by LA-MC-ICPMS

Boron exists as two aqueous species in seawater, boric acid (B(OH) $_3$) and borate ion (B(OH) $_4$). At a salinity of 35 the boron concentration in seawater is \sim 433 µmol kg $^{-1}$ and, due to its long seawater residence time, is well mixed (Lee et al. 2010). The relative abundance of the two aqueous species is pH dependent (Fig. 1; Dickson, 1990). There are two naturally occurring isotopes of boron, 10 B and 11 B, and boron isotope variations are described in delta notation:

$$\delta^{11}B = \left(\frac{^{11}B/^{10}B_{Smp}}{^{11}B/^{10}B_{Std}} - 1\right) * 1000 \tag{1}$$

where $^{11}\text{B}/^{10}\text{B}$ is the ratio of ^{11}B to ^{10}B in the sample (Smp) and standard (Std), which in this case is NIST SRM 951 ($^{11}B/^{10}B = 4.04367$; Catanzaro et al., 1970). The structural differences between boric acid and borate ion cause an isotopic fractionation to exist between the two aqueous species of 27.2 ‰ (Klochko et al. 2006), such that as the abundance of the species changes their isotopic composition must also vary in order to keep the isotopic composition of total boron constant (39.61 %; Foster et al. 2010; Fig. 1). Although the exact mechanism of boron incorporation into CaCO₃ is the subject of ongoing research, it is thought that the charged borate species dominates (Hemming and Hanson, 1992). In calcites in particular, a secondary fractionation related to precipitation rate may also exist (Farmer et al., 2019) although such fractionations are not always seen in biogenic calcites (e.g. Rae et al., 2011). These issues aside, because incorporation of the borate species is dominant the boron isotopic composition of marine carbonates largely tracks the pH of the fluid they precipitated in, via this equation (Zeebe and Wolf-Gladrow,

$$pH = pK_B - log\left(-\frac{\delta^{11}B_{sw} - \delta^{11}B_{CaCO3}}{\delta^{11}B_{sw} - \alpha_B \times \delta^{11}B_{CaCO3} - 1000 \times (\alpha_B - 1)}\right)$$
(2)

where $\delta^{11}B_{sw}$ is the isotopic composition of seawater (39.61 ‰, Foster et al., 2010), pK_B is the -log_{10} of the K_B, the boron dissociation constant (a function of temperature, salinity and pressure; Dickson, 1990). Here salinity is assumed to be 33, pressure 1 atm, and temperature is provided by the temperature logger in Loch Sween since 2004 (Mao, 2019). α_B is the isotopic fractionation factor (1.0272; Klochko et al., 2006) and $\delta^{11}B_{CaCO3}$ is the measured boron isotopic composition of the calcium carbonate.

In scleractinian corals, the pH skeletal aragonite $\delta^{11}B_{CaCO3}$ records is thought to be that of the calcifying fluid, that is itself a function of seawater pH (e.g. Holcomb et al. 2014). Whereas in foraminiferal calcite, the pH recorded by $\delta^{11}B_{CaCO3}$ is thought to be that of seawater (Rae et al., 2011) or their diffusive boundary layer (Henehan et al. 2016). Why these distinct behaviours exist is currently unknown but may relate to the degree of boron enrichment in the calcifying fluid from boric acid diffusion (Gagnon et al. 2021). For CA the existing $\delta^{11}B$ data largely overlaps with coral $\delta^{11}B$ (Fig. 1), leading most previous authors to interpret the CA $\delta^{11}B$ -derived pH data in terms of internal pH (e.g. Cornwall et al., 2017; McCoy et al. 2023), even though CA are also characterised by elevated pH in their diffusive boundary layer due to photosynthesis (e.g. Hurd et al., 2011).

2.3. Mass spectrometry and geochemical imaging

Boron isotope analyses were performed on a Thermo Scientific (Thermo Fisher Scientific, Waltham, MA, USA) Neptune Plus multicollector (MC)-ICP mass spectrometer coupled to an Elemental Scientific Lasers (Bozeman, MT, USA) NWR193 excimer laser ablation system with a TwoVol2 ablation chamber. Analytical protocols broadly followed Chalk et al. (2021) and Standish et al. (2024). ¹⁰B and ¹¹B were measured on the L3 and H3 Faraday cups installed with $10^{13}\,\Omega$ resistors. Potential surface contamination was removed prior to data collection by ablating the sample and standard surfaces with a low laser power density ($\sim\!1$ J cm $^{\!-2}\!)$ and fast laser tracking speed and repetition rate (200 μm s⁻¹ and 20 Hz, respectively). Operating conditions during data acquisition are detailed in Table S1. Samples and standards were ablated in line-mode. Data were collected in static mode, with each standard analysis consisting of 100 integration cycles of 2.194 s (ca. 2.2 mm in length). The sample analyses consisted of 20 parallel and adjacent ablation transects with a laser beam size of 50 µm diameter, with each transect consisting of ca. 142 cycles of 2.194 s integration cycles. This resulted in an ablated area ca. 1 by 3 mm. Dynamic blank corrections were applied cycle by cycle assuming a linear relationship between the preceding and succeeding blank measurements, and instrumental mass bias was corrected by standard-sample bracketing with NIST SRM610 glass reference material and the isotope composition published by Standish et al. (2019). Matrix interferences from scattered Ca ions (see Standish et al. 2019) were corrected for based on a power-relationship (Evans et al., 2021) between $\delta^{11}B$ inaccuracy and $\hat{}^{11}B$ /interference of carbonate reference materials JCp-1, Porites sp. coral and JCt-1, Tridacna gigas clam (Inoue et al., 2004; Gutjahr et al., 2021), where the interference was measured at m/z of 10.10. Standard and sample data were screened and cycles falling outside of 2SD (standards) or 3SD (samples) of the mean were removed.

Internal reference material PS69/318–1, a fragment of cold-water coral, was ablated throughout the analytical session as a guide to internal precision, external reproducibility and accuracy. Internal precision, expressed as 2 SE of the mean of the 100 integration cycles, was \leq 0.6 ‰. The mean δ^{11} B of the repeat analysis of PS69/318–1 (n=3) was 14.3 \pm 0.5 ‰ (2 SD; Table S2), consistent with a solution measurement of 13.83 \pm 0.29 ‰ (2 σ ; Standish et al., 2019).

E/Ca element analysis was performed on a Thermo Scientific X-Series II Quadrupole ICP mass spectrometer coupled to an Elemental Scientific Lasers NWR193 excimer laser ablation system with a TwoVol2 ablation chamber. Samples and standards were ablated in line-mode and analysed for ⁷Li, ¹¹B, ²⁴Mg, ⁴³Ca, ⁸⁶Sr, ¹³⁷Ba, and ²³⁸U to enable calculation of E/Ca ratios. Standard analyses consisted of ca. 680 integration cycles of 0.173 s (ca. 1.2 mm lines), whilst sample analyses which ablated the same area as analysed by LA-MC-ICPMS (20 adjacent ca. 3 mm long ablation transects), consisted of \sim 1730 integration cycles of 0.173 s. Operating conditions are detailed in Table S1. On-peak blank corrections were applied based on the mean intensities of preceding and succeeding blank measurements. Instrumental drift and mass bias were corrected by standard-sample bracketing with NIST SRM612 and the values from the interlaboratory comparison study of Jochum et al. (2011). Standard and sample data were screened and cycles falling outside of 2SD (standards) or 3SD (samples) of the mean were removed.

In-house reference material PS69/318–1 was ablated throughout the analytical session as a guide to internal precision, external reproducibility, and accuracy. Internal precision, expressed as 2 SE of the mean of the total number of integration cycles, was \leq 5% for all ratios (see Table S2). External reproducibility, expressed as 2 SD of the mean of 3 analyses, was \leq 5% for all ratios. Mean accuracy of all ratios is to within 13% relative to measurements by solution ICP-MS for Li/Ca, B/Ca, Mg/Ca, Sr/Ca, Ba/Ca, and Li/Mg, and within 26% for U/Ca.

The construction of isotopic and elemental maps from these trace element and boron isotope data was performed in R (R, 2010) using an adapted script from Chalk et al. (2021) and the Raster package (Hijmans,

2022). Each laser line for Li/Ca, B/Ca, Mg/Ca, Sr/Ca, U/Ca and $\delta^{11}B$ was subjected to a 3SD to remove any outliers before a moving average was used to smooth the data. The width of the moving average window was 5 points for both TE/Ca and 3 points $\delta^{11}B$ to reflect their differing integration times. The sets of 20 smoothed laser lines were mapped onto an equal spaced grid using their X and Y spatial coordinates from Elemental Scientific Lasers NWR193 excimer laser ablation system using the Raster package (Hijmans, 2022). The pixel size of the images produced was approximately $2.1 \times 50~\mu m$ per pixel for the TE/Ca and $25 \times 50~\mu m$ for the $\delta^{11}B$. The actual resolving power of the images in the direction of travel is less than the pixel size (2.1 um and 25 um for the TE/Ca and $\delta^{11}B$ images, respectively) due to: i) the 5 and 3 point smoothing we applied; ii) mixing at the scale of the spot (as discussed in, for e.g., Fox et al., 2017); iii) signal mixing during aerosol transportation (as discussed in, for e.g., Aonishi et al. 2018).

2.4. Correlative imaging

Datasets were imported into Dragonfly 2022.1 (Object Research Systems, Montreal) as individual tiff images. Both a pre- and postablation SEM image of CS9 were imported, with the two images aligned using Dragonfly's automated image registration tool, specifically the implementation of a rigid Maximisation Of Mutual Information (MMI) algorithm (Fig. 2a–c).

Once aligned, the pre-ablation SEM image was further manually segmented into subsets (similar to Standish et al., 2024), to separate pixels most clearly associated with the central and marginal parts of the skeleton using Dragonfly's ROI painter tool (Fig. 2d). Each pixel assigned to the central parts of the skeleton (displaying clear light-dark banding) was allocated a pixel intensity of 1, each pixel attributed to the marginal skeleton (near the skeletal margins where banding was largely absent) a pixel intensity of 2, background pixels an intensity of 3, and the outermost skeleton, which represents the epithallus and therefore likely contained remnant tissue, was assigned an intensity of 4.

This alignment of pre- and post-ablation SEM images allowed the ablation scar left following TE/Ca and $\delta^{11}B$ mapping to guide the alignment of the TE/Ca and $\delta^{11}B$ maps to the SEM. For this second alignment, the ablation scar from the post-ablation SEM image was segmented using Dragonfly's ROI painter, and the TE/Ca and $\delta^{11}B$ maps were imported as an image stack. Again, MMI was used to align the map dataset to this ablation area (Fig. 2e), with the TE/Ca and $\delta^{11}B$ datasets then resampled to match the dimensions of the SEM, preventing downsampling of the SEM resolution (Fig. 2f).

The creation of a pixel classifier image allowed the sub-setting of the skeleton of CS9, including the associated TE/Ca and δ^{11} B maps and preablation SEM greyscale values indicative of skeletal density (Fig. 2g).

2.5. Depth, time series, extension rate and rate of calcification

Once aligned and segmented, the data (including the greyscale values of the SEM image and pixel classifying image) most closely corresponding to the central growth axis were selected (Fig. 2h). This was done by further subsetting the aligned dataset to only include the rightmost 26 columns of pixels. As discussed above, all the images were resampled to the resolution of the SEM image to retain the visible density banding, and so for the TE/Ca and $\delta^{11}B$ maps this equates to the rightmost 4 ablation lines. These were then averaged and a standard error calculated with n = 4 to reflect the original resolution of the dataset (except for the SEM where n = 26). These average values were then plotted vs. depth and a preliminary age model was constructed using the time of collection (March 2018) and the light/dark banding evident on the aligned SEM image and depth series where each light/ dark pair represents 1 year of growth with the SEM-dark bands (i.e. the low density) growing during the warmer months of the year (Kamenos and Law 2010). This preliminary age model was then refined further by tuning the Mg/Ca variation to Loch Sween logger temperature (see

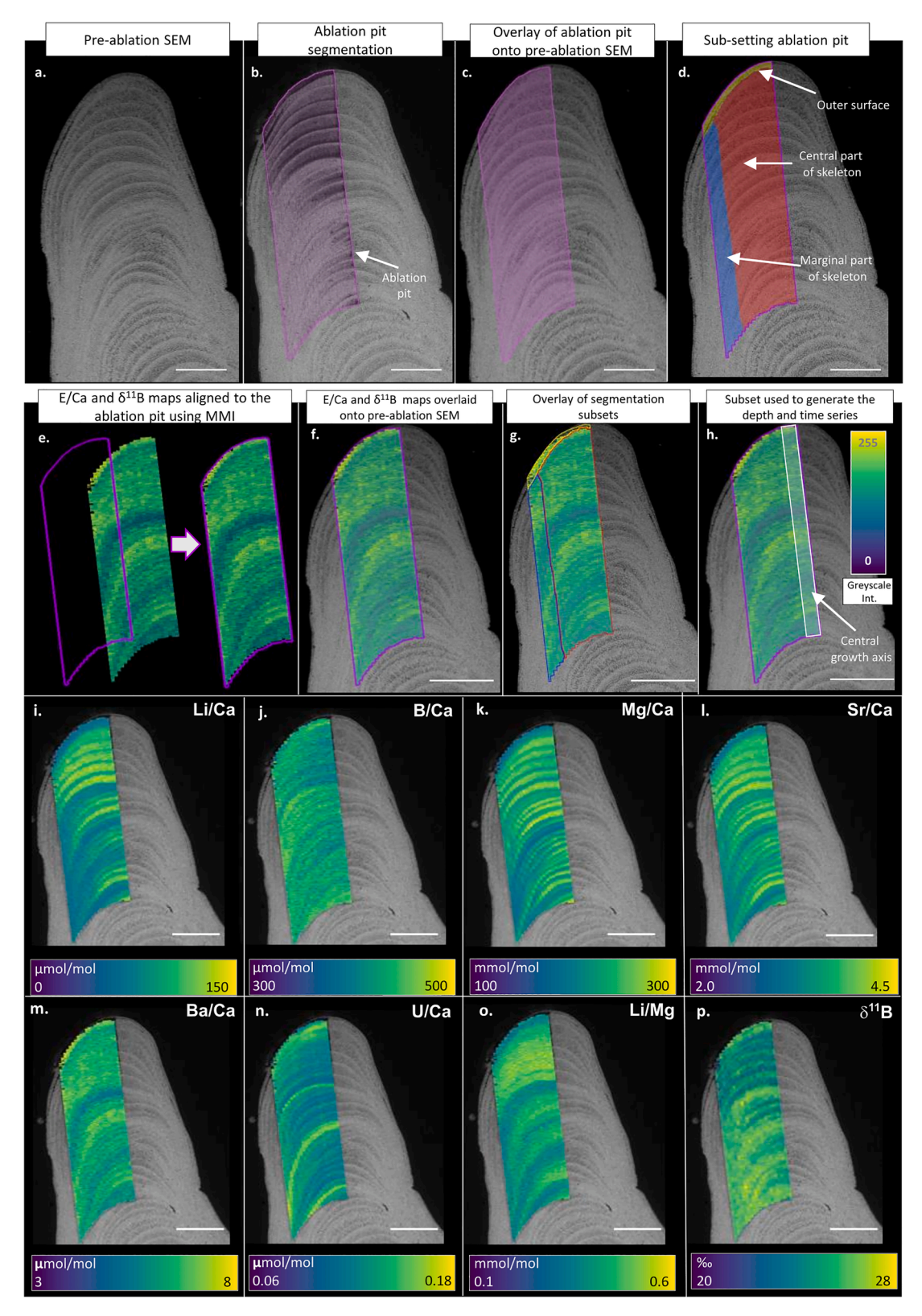


Fig. 2. Correlative imaging of *B. soriferum* sample CS9. (a) pre-ablation SEM image of CS9. (b) post ablation SEM image of CS9. (c) Overlay of pre- and post-ablation SEM image of CS9. (d) Manual sub-setting of the ablated area into central and marginal portions and the outermost surface layer. (e, f and g) the steps associated with the alignment of the different imaging modalities and, once aligned, the transference of the manually sub-setted area to the aligned geochemical maps. (h) The area isolated as the central growth axis for constructing the depth and time series shown in Figs. 4 and 5 is illustrated as a white box. This box is 26 pixels wide. (i) Li/Ca map (μ mol/mol), (j) B/Ca map (μ mol/mol), (k) Mg/Ca map (μ mol/mol), (l) Sr/Ca map (μ mol/mol), (m) Ba/Ca map (μ mol/mol), (n) U/Ca map (μ mol/mol), (o) Li/Mg map (μ mol/mol), (p) μ mol/mol), (s) Scale bars in each image are 750 μ m.

Section 2.1), assuming the positive relationship between these variables seen in other studies of this species (Kamenos et al., 2008). Peak, trough and midpoint (where growth rates allowed it) of each time series were used as tie points using the astrochron package in R (Meyers, 2014). From the resultant depth-time relationship, the amount of skeleton grown at each time step was determined, allowing an extension rate (in µm/year) to be calculated for the line of section. Calcification rate (in g/cm²/yr) is the product of density (g/cm³) and the rate of extension (cm/yr; e.g. see Lough et al., 2016). Here we do not have an absolute measure of skeletal density, but because the skeleton is grey and the pores are black (or near black) when imaged using SEM, when averaged over multiple pixels SEM greyscale reflects the macro-porosity of the skeleton (e.g. Chalk et al. 2021) and thus is a measure of skeletal macro-density. Greyscale variations in the SEM image may also reflect material density, but we do not consider that here. We are therefore able to calculate a relative calcification rate by multiplying normalised SEM greyscale by the normalised linear extension rate determined by our age model. Although care was taken to section the sample perpendicular to its main growth axis, it is possible that the direction of maximum extension is not captured by our plane of section. However, Yudelman and Slowey (2022) suggest this phenomenon is unlikely to unduly bias the estimates of extension calculated in this way. Seasonal cycles were extracted from the timeseries generated by first removing the long-term trend defined by a Lowess smoother in R.

Monthly averages of the published ocean pH and aqueous pCO $_2$ timeseries from the Stonehaven and L4 observatories (Fig. S1; Ostle et al., 2016) and Loch Sween logger data were made using the Zoo

Package in R (Zeileis and Grothendieck, 2005).

3. Results and discussion

3.1. 2D geochemical images and observed geochemical variation

The aligned geochemical images are shown in Fig. 2 and Video 1, and the unaligned and aligned data can be found in Tables S3 and S4, respectively. There is a clear visual correlation between the dominant geochemical variability and skeletal variation visible on the SEM image, with well-defined annual banding in the majority of geochemical variables coincident with the SEM-light/SEM-dark growth banding (Fig. 2). It is also evident in the SEM image that the annual banding is most clearly expressed in the central part of the skeleton but towards the margins that banding is obscured, and the skeleton is more dense (lighter SEM; Fig. 2). From a simple visual comparison between the geochemical variation and these differences in banding it appears that the composition of the denser, un-banded margins of the skeleton is different to the majority of the banded skeleton. It is also evident that in several places the high-density (SEM light) skeleton on the margins continues into the main growth axis, at which point the light-dark annual growth banding appears disrupted (Fig. 2). Similar departures in chemical composition (most notably in Ba/Ca) can also be seen in the outermost layer, the epithallus, that is inhabited by living tissue (Fig. 2m). To explore the chemical and isotopic composition of these features in more detail we segmented the SEM image and translated this segmentation to all the aligned geochemical images (Fig. 2). Given that

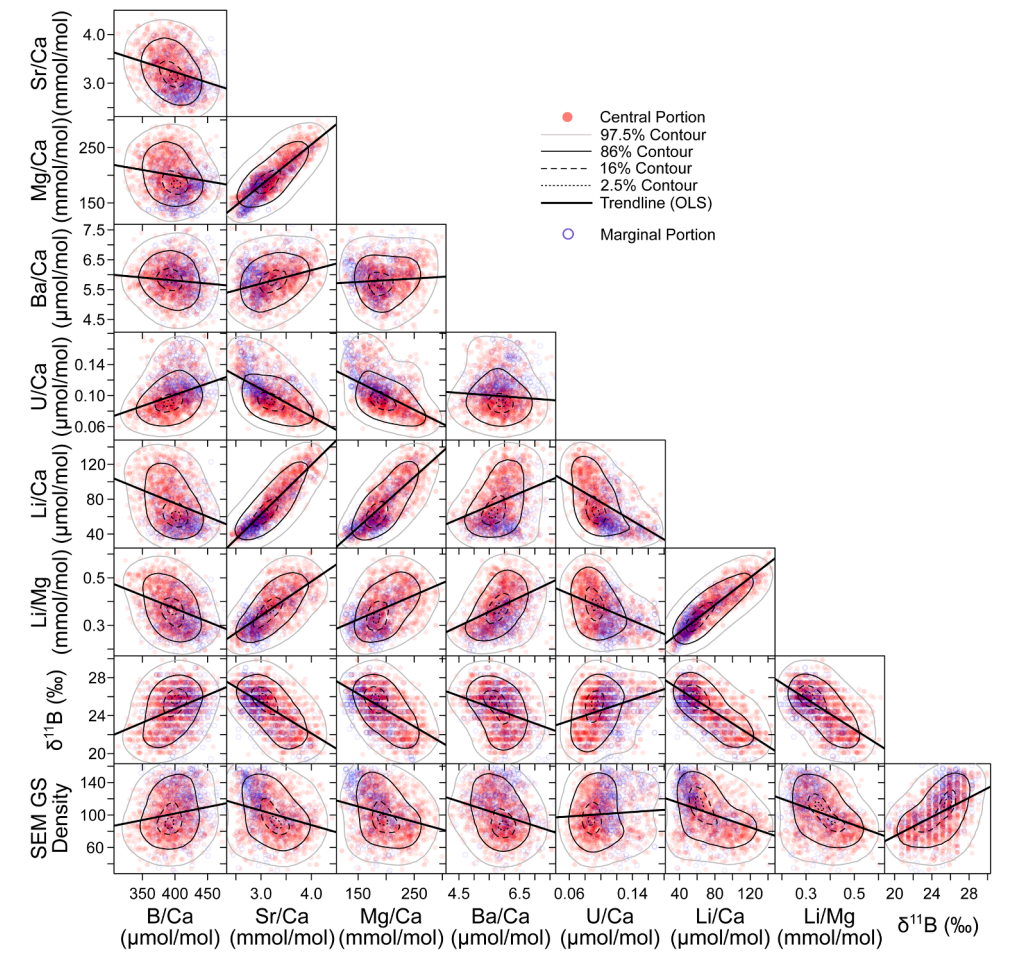


Fig. 3. Cross plots of E/Ca and δ^{11} B in sample CS9. Data for the central and marginal parts of the skeletal are coloured red and blue respectively. Data for the central portion are contoured for upper and lower 95% and 68% confidence (black and grey lines, respectively). Note for clarity only 5% of the data points are plotted. Ordinary least squares best fit lines are also shown and in all cases p values for these regression are <<0.05.

all the images were on the same X-Y grid we are then able to extract the pixel values of the various segmented regions and cross plot them to fully explore the geochemical and skeletal co-variation (Fig. 3). This confirmed what is evident in the 2D images (Fig. 2), that there is considerable the geochemical co-variability in the central part of the skeleton, with Mg/Ca, Sr/Ca, δ^{11} B, and Li/Ca in particular showing strong correlations. Weaker, but significant, correlations are also seen with B/Ca and U/Ca and SEM greyscale (a proxy for skeletal density). The marginal parts of the skeleton (shown in blue in Fig. 3) tend to cluster at one end of any arrays defined by the more central portion. The denser parts of the skeleton of B. soriferum from Scotland form during the winter when the rates of extension are low (Kamenos and Law, 2010). Given the continuation of chemical composition between what is found in winter in the central portion and the composition of the denser skeletal margin, we propose that there has been additional precipitation of CaCO₃ on the margins, and within certain parts of the central growth axis of the skeleton. Given the geochemical similarity to winter grown CaCO₃, it is possible this occurs during several winter intervals. However, this will need further study to confirm it is the case. Regardless, although the causes of this remain unclear at this stage, for the rest of the data analysis here we will not consider these, or the outermost, portions of the skeleton and focus on the well-banded $CaCO_3$ within the central parts of the skeleton (Fig. 2d).

3.2. Time series of pH_{cf} and seasonal cycles of calcification rate and skeletal density

The data from the central growth axis (Fig. 2h) were averaged and plotted as a depth series in Fig. 4. The data itself can be found in Table S5. Using Mg/Ca, a consideration of the SEM-light/SEM-dark growth banding and the temperature logger data from Loch Sween, we placed these data into an age framework (Fig. 5& Table S6). Calcifying fluid pH (pH_{cf}) shows clear seasonal cycles with low pH in the warm summer months and high pH in the winter (Fig. 5), superimposed upon a gradual long-term decline of 0.021 pH units per year. Note, this same sense of seasonal variation is evident in the δ^{11} B data (Fig. 4), so this seasonal cyclicity is not simply imparted by the temperature data used to calculate pH from δ^{11} B (equation [2]). There is a close correspondence between pH_{cf} and skeletal density from SEM greyscale (R² = 0.46; p<<0.05) on both the seasonal scale and the long-term (Fig. 5), forming a well-defined correlation when cross plotted (Fig. 6). Extension rates range from ~100 to ~300 µm/yr and are inversely correlated to

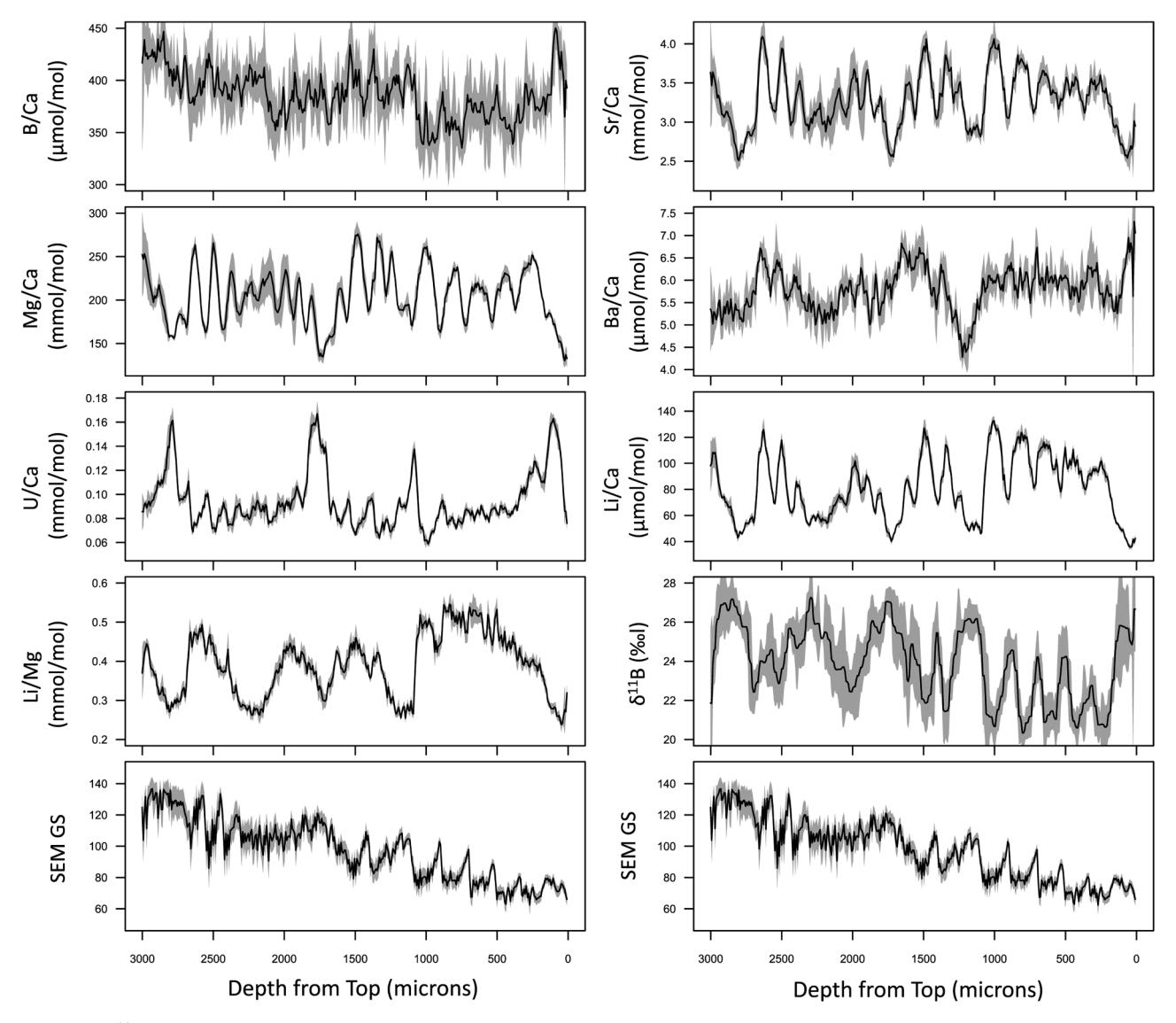


Fig. 4. E/Ca and δ^{11} B in sample CS9 against depth for data from the central growth axis. The grey band in each line is \pm 2SE of the mean and SEM GS is the grey scale values of the SEM image over the same area averaged for the E/Ca and δ^{11} B data. SEM grey scale is a measure of skeletal macro density/porosity (high values = more dense).

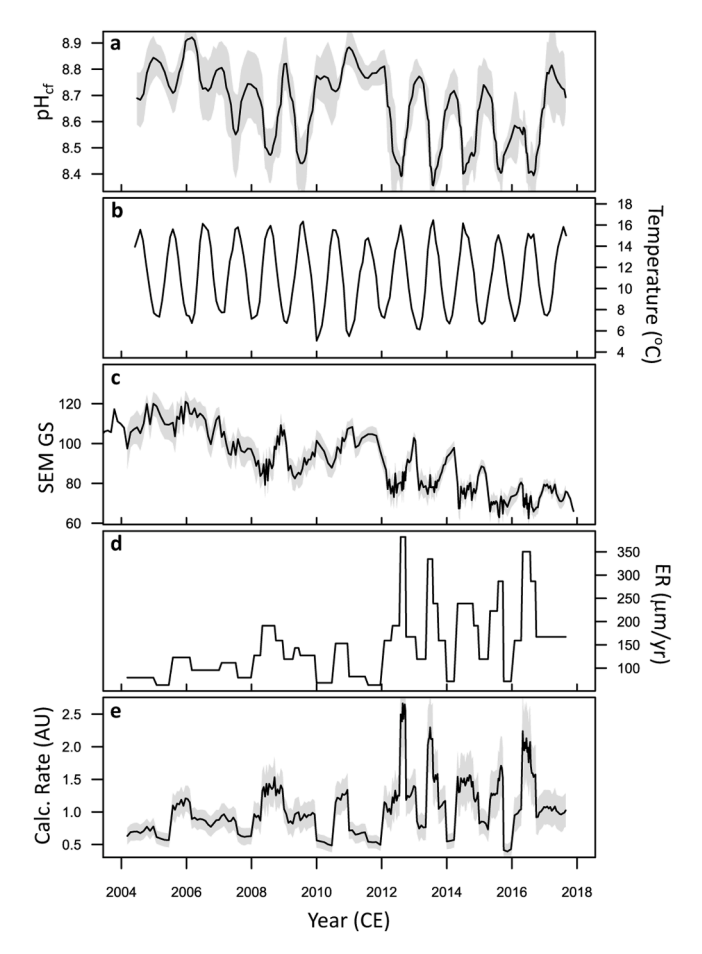


Fig. 5. Time series of calcification and environmental data from the central growth axis of sample CS9. (a) calcification fluid pH (pH_{cf}) determined from $\delta^{11}B$ and equation [2]; (b) logger temperature from Loch Sween; (c) greyscale values of the SEM image which is a measure of skeletal macro density/porosity (high values = more dense); (d) rate of linear extension in μ m/yr.; (e) relative calcification rate (in arbitrary units) calculated as described in text. Grey band is 95% confidence uncertainty band.

 pH_{cf} and skeletal density, both on the long-term and short-term, being higher by about a factor of 2–3 during warm vs. cold seasons. Calcification rate closely corresponds to extension rate showing similar seasonal variations (Fig. 5) and is inversely related to pH_{cf} (Fig. 6).

In tropical corals, calcifying fluid pH is also seen to be inversely correlated with temperature, with a slope that is similar to our B. soriferum data when either considering the dataset as a whole, or just the well-banded portions of the central growth axis (Fig. 6). To explore the effect of seawater pH on pH_{cf}, we follow D'Olivo et al. (2019) and attempt to normalise the pH_{cf} to a single temperature to remove this temperature dependency. This can be achieved by using the slope of the temperature to calcifying fluid pH relationship (Fig. 6) defined by the well-banded data from the central growth axis (-0.032 pH units per $^{\circ}$ C) and multiply this by the ΔT , the difference between the temperature at time t and the mean temperature for the time series. Given we have seawater pH logger data for 2014 from Loch Sween, we can then isolate this portion of the CS9 time series and regress pH_{sw} against temperature normalised pH_{cf} (Fig. 7 and Table S7). This indicates that pH_{cf} = pH_{sw} * 0.73 ± 0.12 , a change in internal pH for a given change in pH_{sw} that is higher than other CA species and that seen in some, but not all, coral species (0.3 to 0.8; e.g. see compilation of Eagle et al. 2022). Taken together it therefore appears that the boron isotope systematics, and hence the behaviour of pH_{cf}, of B. soriferum is very similar to that seen for tropical corals (Figs. 1 and 7). Whether this is due to the existence of the similar biomineralisation mechanisms is currently unknown, although this has previously been speculated to be the case (e.g. Cornwall et al. 2017).

To the best of our knowledge, the boron isotope composition of inorganically produced high-Mg calcite has yet to be determined. Experiments that have been carried out with calcite show that, in contrast to abiogenic aragonite, there are significant offsets between the $\delta^{11}B_{CaCO3}$ and $\delta^{11}B$ of borate. Using surface kinetic modelling, Farmer et al. (2019) propose this arises either from a precipitation rate dependent incorporation of boric acid or kinetic isotope fractionation of the borate ion during incorporation. While those authors favour the former process, it remains debatable as to how much of this inorganic effect is expressed by biogenic calcites such as foraminifera (e.g. Rae et al., 2011). A prediction of the model proposed by Farmer et al. (2019) is that as the precipitation rate decreases the degree of positive fractionation of calcite from borate increases and the concentration of boron is reduced. Therefore, if such rate dependent fractionation was controlling the

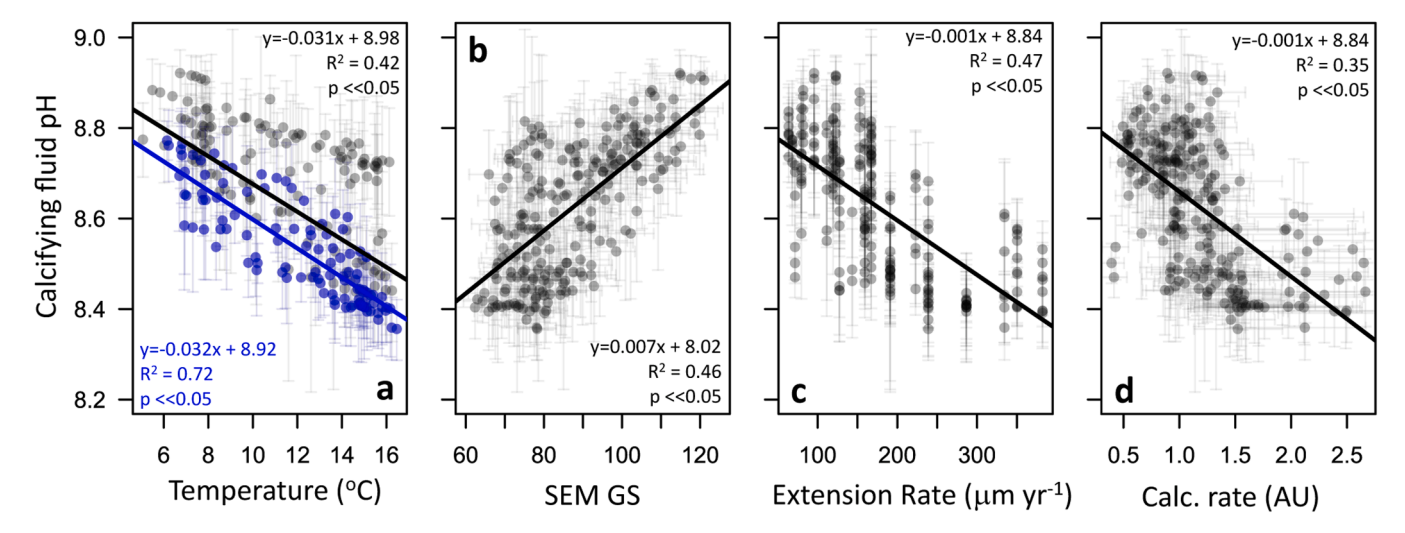


Fig. 6. Relationships between key calcification metrics from the central growth axis. (a) pH of the calcifying fluid in CS9 determined from $\delta^{11}B$ and equation [2] plotted against coeval logger temperature from Loch Sween. Data from well-banded portions of the skeleton are shown in blue, all other data in grey. (b) calcifying fluid pH against SEM grey scale which is a measure of skeletal density (high values = more dense); (c) calcifying fluid pH against rate of linear extension in μ m/yr; (d) calcifying fluid pH against relative calcification rate (in arbitrary units). In all cases 95% confidence error bars are shown. Ordinary least squares best fit lines shown along with relevant statistics.

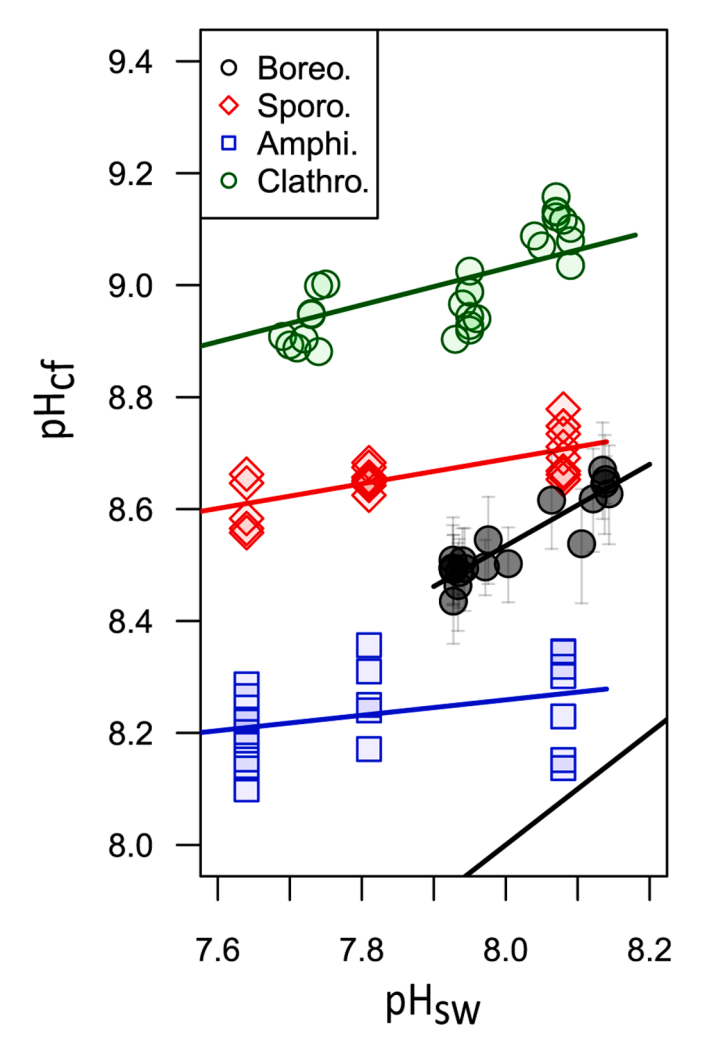


Fig. 7. The relationship between calcifying fluid pH and seawater pH for a range of coralline algae including data for CS9 (summarised in Table S7). Published data are shown as coloured symbols and data for CS9 Boreolithothamniom soriferum (Boreo.) determined here are show as grey circles, with associated 95% confidence intervals. Sporolithon durum (Sporo.) and Amphiroa anceps data from Cornwall et al. (2017) and Clathromorphum compactum (Clathro.) data from Anagnostou et al. (2019). 1:1 line shown in black and best fit lines from ordinary least squares shown in appropriate colour and labelled with slope (m).

boron systematics here, higher $\delta^{11}B$ should be associated with lower B/Ca and this should occur when calcification rates were lowest. While lower calcification rates are associated with higher $\delta^{11}B$ in our B. soriferum, B/Ca is positively correlated with $\delta^{11}B$ rather than negatively correlated (Fig. 3). Also, the range in precipitation rate in the model of Farmer et al. (2019) required to drive the \sim 8 per mil variation in $\delta^{11}B$ exhibited here by B. soriferum is >3 orders of magnitude which is much larger than the 2–3x variations we observe (Fig. 5).

If these isotope rate effects are not of sufficient magnitude to drive the variations in B. soriferum $\delta^{11}B$ and hence pH_{cf} drawing on the available literature for corals, we are left with two principal explanations: either the cycles in pH_{cf} result from environmentally driven variations in CA physiology (e.g. Cornwall et al., 2017) or they arise from the combined effect of seawater chemistry and temperature on the rate of calcification and calcifying fluid buffering capacity (Guo, 2019). Given that the patterns are similar between the scleractinian corals and our B. soriferum as well as other CA, we favour the latter hypothesis. If this is the case, then the seasonal cycles in pH_{cf} we observe are caused by: (i) the buffering capacity of seawater being reduced at lower

temperature which is an abiogenic effect that causes pH (but notably not CO_3^{2-}) to be lower at higher temperature for a given DIC and ALK, and (ii) the production of 1 mole of CaCO3 removes 1 mole of DIC and 2 mol of ALK, causing the pH_{cf} (and CO_3^{2-}) to decline. The rate of inorganic calcite precipitation is a strong function of temperature (Burton and Walter, 1987) so higher temperatures result in more calcite precipitation in the calcifying space at any given time. The close correspondence between pH_{cf}, calcification rate and temperature on seasonal time-scales provides strong support for the importance of this process (Fig. 8). Skeletal density reflects the combined effect of the rate of calcification and the rate of extension, and as Fig. 8 shows, skeletal density is lowest when temperature is warmest, this is because although calcification rate is higher when temperatures are higher (Fig. 8), the rate of extension is great enough to result in the enhanced CaCO3 precipitation to be distributed over a great area per unit time, causing a less dense skeleton (Fig. 8). A similar inverse relationship between skeletal density and temperature, and a positive relationship between rate of extension and temperature has been noted before in this species (then Lithothamnion glaciale) by Kamenos and Law (2010).

3.3. Ocean acidification and pCO₂ change at Loch Sween

From 1982 through to 2021, recent compilations suggest the pH of the global surface ocean has declined at a rate of -0.0166 ± 0.001 per decade (Ma et al., 2023), with open ocean rates around the UK slightly lower than the global mean (ca. -0.015 per decade). The shelf seas around the UK, like in many areas of shallow water close to the continents, display considerably more spatial and temporal variability than the open North Atlantic (Findlay et al. 2022; Carstensen and Duarte, 2019). Observations are however sparse, with long-term monitoring restricted to two locations: Marine Science Scotland's Stonehaven station located 5 km off the east coast of Scotland, and Plymouth Marine Laboratory's Western Channel Observatory station L4, 7 km off the southwest coast of southern England (Fig. S1), that have been measuring pH weekly since 2008 (although only data from 2008 to 2015 are currently publicly available). Despite the considerable inter-annual variability, both stations show similar seasonal dynamics in carbonate system: generally lower pH in the winter, and higher pH in the summer thought to be driven by a combination of temperature and biological activity (e.g. seasonal variations in the balance between net ecosystem calcification and net ecosystem primary productivity; Findlay et al. 2022). Although we only have a little under a year of pH data from Loch Sween, a similar pattern is seen albeit with peak pH occuring during the spring with a broad pH minimum extending from late summer to early winter (Fig. S2).

Using the pH_{sw} to temperature corrected pH_{cf} relationship we established above (Fig. 7), we can estimate pH_{sw} from our pH_{cf} record for the interval 2004 to 2017 (Fig. 9 and Table S8). Note we have removed the dense skeletal deposits that extend from the skeleton margins from this analysis to better isolate a primary pH_{sw} signal. As expected, the agreement for the year where we have logger pH is very good. Outside of the calibration interval overlap with the Stonehaven and L4 data is also very good (Fig. 9). In terms of long-term trend, for Loch Sween we record a rate of -0.025/year for the entire record, and -0.018/year for the 2008-2014 interval that temporally overlaps with the Stonehaven data. These trends are compared to L4 and Stonehaven in Table S9, and although L4 appears to be acidifying slower than the Loch Sween, there is good agreement between our $\delta^{11}B$ -derived rates of ocean acidification and the observations from Stonehaven (-0.019/ year). Notably, as others have found (e.g. Carstensen and Duarte, 2019) these coastal locations are acidifying an order of magnitude faster than the nearby open ocean. While the cause for this is currently unclear, it may involve long-term trends in riverine nutrient supply to the coastal locations as has been proposed elsewhere in Europe (Cartensen and Duarte, 2019) and is evident in the UK (Worrall et al., 2016).

To calculate the effect of this ocean acidification on seawater pCO₂

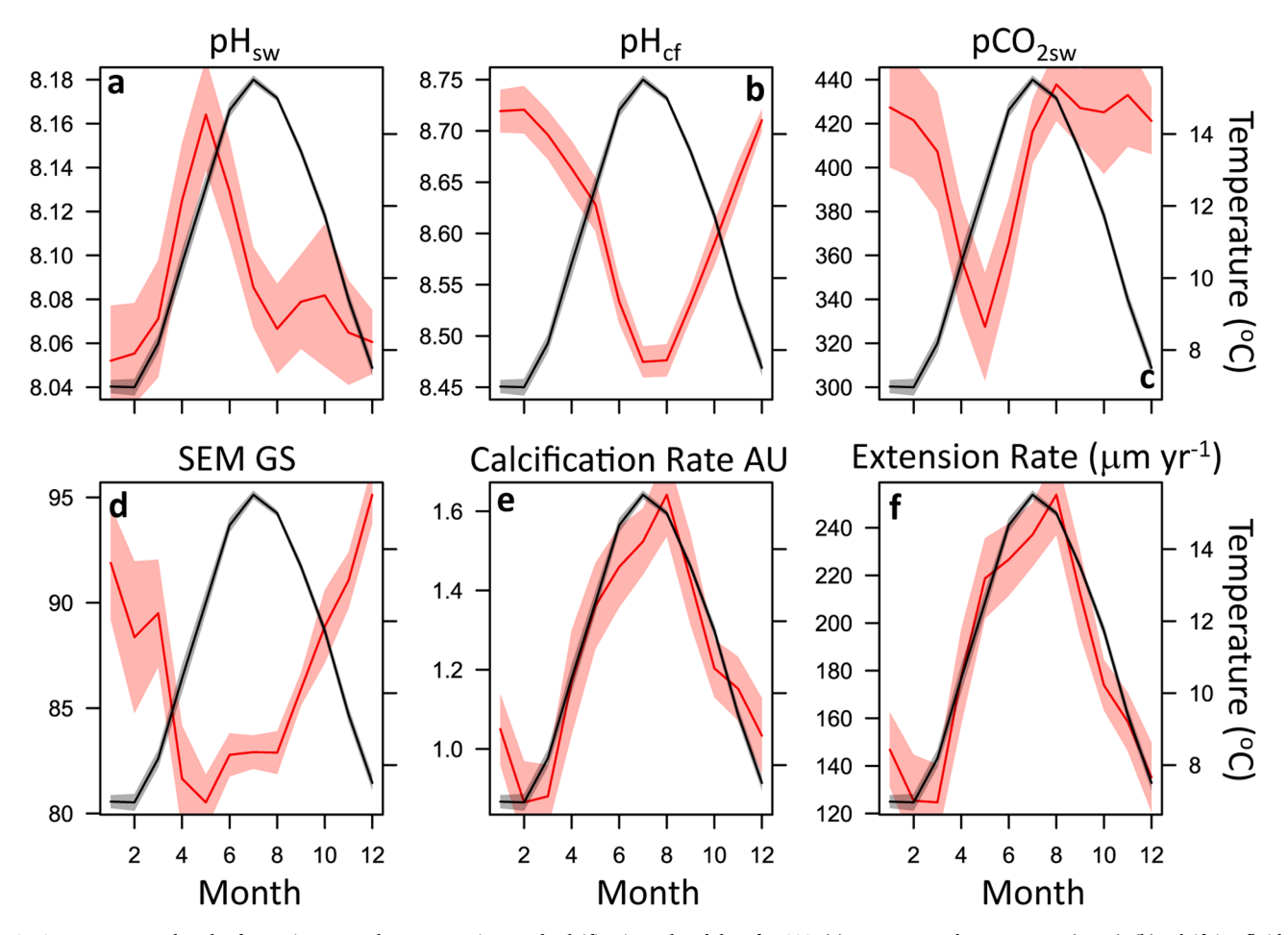


Fig. 8. Average seasonal cycles for environmental reconstructions and calcification related data for CS9. (a) reconstructed seawater pH (pH_{sw}); (b) calcifying fluid pH calculated from $\delta^{11}B$ and equation [2]; (c) reconstructed seawater pCO₂ (pCO_{2sw}); (d) SEM grey scale which is a measure of skeletal density (high values = more dense); (e) relative calcification rate in arbitrary units; (f) rate of linear extension in μ m/yr. In all cases the seasonal cycle in logger temperature from Loch Sween is shown in black and the relevant dataset is shown in red. 95% confidence error bands are shown as shaded bands of the appropriate colour.

(pCO_{2sw}) at Loch Sween we need an estimate of ALK, which was measured as 2243-2261µmol kg-1 during a study that took place between 14/05/2019-16/05/2019 (MacDonald et al., in review). As discussed in Hain et al. (2018), uncertainty in ALK does not contribute substantially to an estimate of pCO2 when pH is known, nonetheless we used a uniform uncertainty of \pm 50 µmol kg⁻¹ here to encompass the likely range. Fig. 9 shows our reconstruction of Loch Sween pCO_{2sw} since 2004 and we see a substantial increase through the record with a trend of $+22.7~\mu atm$ per year, similar to the trend at Stonehaven ($+19.3~\mu atm$ per year) but higher than that at L4 (+6.4 µatm per year; Table S3; Table S8). As with the rates of pH change, these rates of pCO_{2sw} increase are around 10x faster than those of the atmosphere (\sim 2.6 µatm per year; Fig. 9). It is notable that prior to ~2008 our reconstruction suggests Loch Sween was a sink of CO₂ (i.e. pCO_{2sw} was lower than atmospheric levels), but post ~2008, particularly during the early summer it was a substantial source, with pCO_{2sw} reaching 600 µatm, nearly 200 µatm above atmospheric levels (Fig. 9). As with pH_{sw}, the seasonal pCO_{2sw} variations we reconstruct (Figs. 8and 9) are likely the result of seasonal changes in ecosystem level biological activity and water temperature.

3.4. Insights into the long-term environmental sensitivity of B. soriferum calcification and growth

As discussed in Section 3.2, the good correlations that we observe between pH_{cf} and SEM-based density and calcification rate suggest the carbonate system within the calcifying fluid of *B. soriferum* plays a key role in skeleton construction (Fig. 6). We discussed in Section 3.1 that

the seasonal temperature cycle was a likely driver of seasonal variability in the pH_{cf}, density, extension rate and calcification rate; pH_{sw} (and pCO_{2sw}) display a seasonal cycle that is quite different to the calcification related properties (Fig. 8). Since there is no significant long-term trend in temperature over the interval from 2004 to 2015 ($m=0.06\pm0.06$, p=0.34), the driver of the long-term trends in calcification, density and pH_{cf} is likely the long-term pH_{sw} decline (Figs. 9and 5).

Ragazzola et al. (2012) examined the cell structure of L. glaciale and showed that cell wall thickness decreased as pCO_{2sw} increased from 422 to 1018 μ atm (a pH change from 8.03 to 7.72). A decrease in skeletal density with ocean acidification has also been seen in a number of other species of CA (e.g. Clathromorphum nereostratum and Clathromorphum compactum; Williams et al., 2021). Skeletal density determined here in CS9 is linearly correlated with seawater pH and seawater pCO₂, with a particularly strong relationship evident in the long-term signal isolated using a Lowess fit (Fig. 10). Finite element modelling from Ragazzola et al. (2012) showed that such an increase in porosity severely weakens the skeleton, suggesting continued ocean acidification at Loch Sween will lead to increasingly porous skeleton for this species with potentially serious impacts on its fitness.

Kamenos et al. (2013) also cultured *B. soriferum* (then L. *glaciale*) at two pH's (8.2 and 7.7) and found that net calcification was higher at the low pH treatment by around a factor of 3. Such a positive relationship between pH and calcification in CA is unusual in the meta-analysis of Cornwall et al. (2022), but 10–15% of CA species display a parabolic response where although calcification initially increases with decreasing pH, at high pH stress calcification rates decline. Our correlations

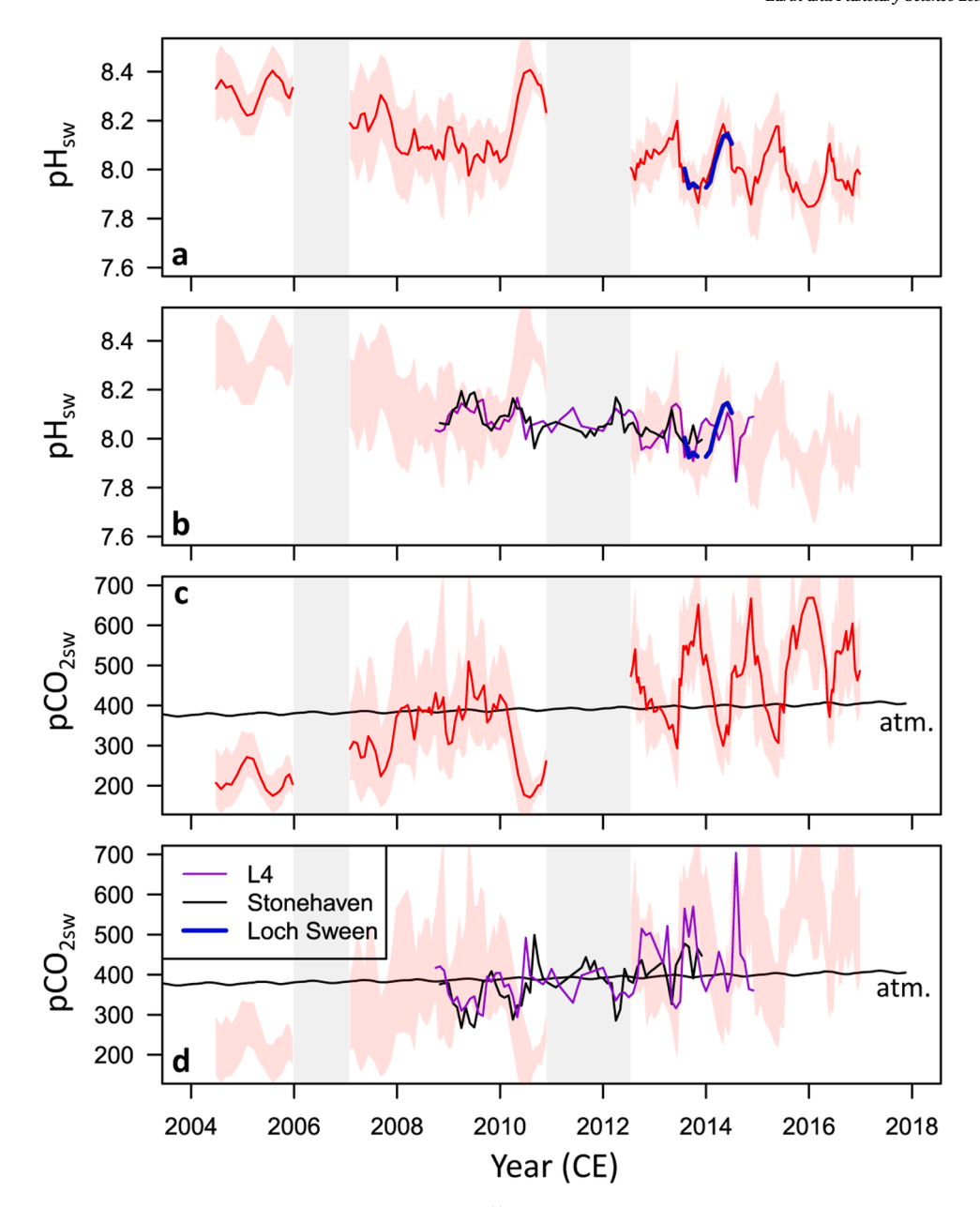


Fig. 9. Time series of carbonate system reconstructions for Loch Sween from the $\delta^{11}B$ data generated on CS9 (data can be found in Table S8). Only the data generated from the well-banded parts of the central growth axis are shown, data from the dense bands that extend from the skeletal margins are removed (grey bands). (a) reconstructed seawater pH (pH_{sw}) for Loch Sween in red with 95% confidence band. In blue are monthly averaged pH logger data for Loch Sween; (b) Monthly averaged pH_{sw} from observation timeseries from UK coastal waters (from Ostle et al., 2016), see Fig. S1 for locations of these stations, a key is in panel (d). 95% confidence band for the $\delta^{11}B$ -based pH_{sw} reconstruction is shown as a red band. (c) reconstructed seawater pCO₂ (pCO_{2sw}) for Loch Sween constructed using $\delta^{11}B$ measured on CS9 and an assumption of total alkalinity (see text for details). A 95% confidence error band is shown. The dotted line is contemporaneous atmospheric pCO₂ measured at Mauna Loa (https://gml.noaa.gov/ccgg/trends/ and https://scrippsco2.ucsd.edu/). (d) reconstructed pCO_{2sw} from Loch Sween shown as 95% confidence band along with monthly averaged logger based pCO_{2sw} from Ostle et al. (2016). See Fig. S1 for station locations. The dotted line is contemporaneous atmospheric pCO₂ measured at Mauna Loa (https://gml.noaa.gov/ccgg/trends/ and https://scrippsco2.ucsd.edu/).

between calcification rate and seawater pH or pCO $_{2sw}$ are significant but their R 2 are very low (0.08; Fig. 10). By isolating the long-term trend from the seasonal cycle using a Lowess fit, it is evident that, as seen by Kamenos et al. (2013), the increasing pCO $_{2sw}$ and decreasing pH $_{sw}$ are well correlated with a decrease in density and increase in extension rate and calcification rate (bold lines in Fig. 10).

Carbon is essential for photosynthesis in macro algae, but in aqueous environments it is often limited, leading to many marine algae using a variety of carbon concentrating mechanisms to actively concentrate $\rm CO_2$ at the active site of RuBisCO. Using carbon isotopes, Bergstrom et al. (2020) showed a range in the extent to which CA rely on diffusive $\rm CO_2$

transfer vs. active pumping. Although *B. sorifierum* was not examined in that study, the congeneric *Lithothamnion proliferum* had a relatively high reliance on CO_2 diffusion (60–70% of its C; Bergstrom et al. 2020) to meet its carbon needs. Mao et al. (2024) recently confirmed the importance of diffusive CO_2 supply for *B. soriferum* calcification using a radioisotope approach, where calcification was severely retarded by an inhibitor of carbonic anhydrase – an enzyme crucial for the hydrolysis of CO_2 . Given that Loch Sween switched from being a sink of CO_2 to being a seasonal source of CO_2 around 2008 (Fig. 9) it is thus possible that the increase in linear extension and calcification and the decrease in skeletal density we observe that begins around this time, is the result of the

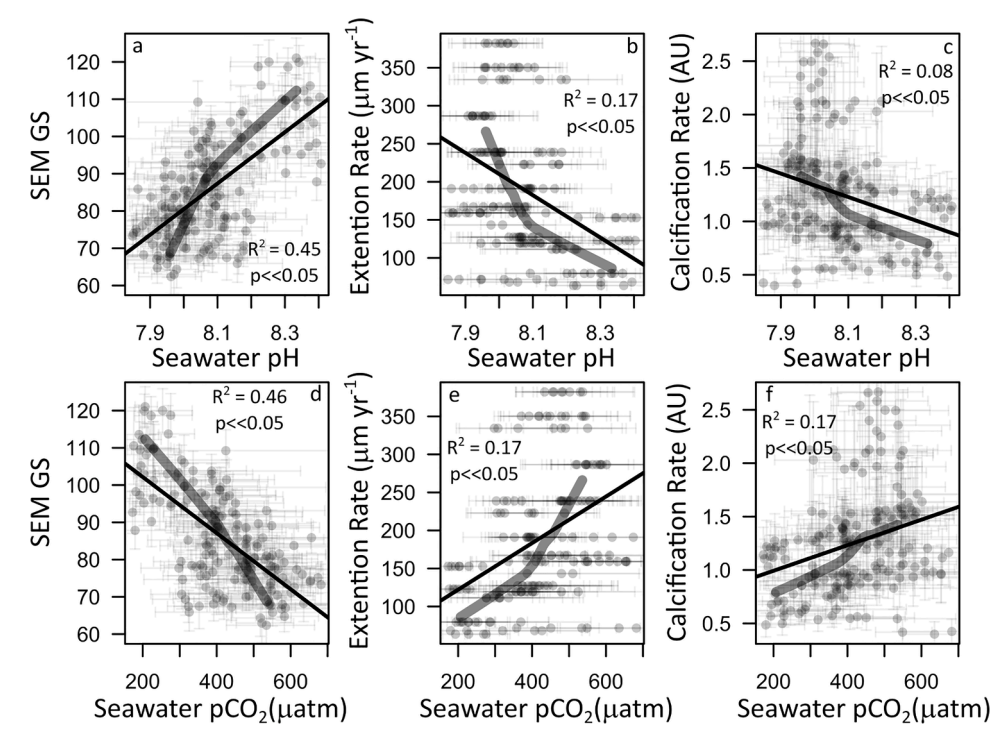


Fig. 10. Relationships between calcification parameters of CS9 with reconstructed carbonate system of Loch Sween. (a) Reconstructed seawater pH vs. SEM grey scale, which reflects skeletal macro density/porosity (high values = higher density). (b) Reconstructed seawater pH vs. the rate of linear extension (in μ m/yr). (c) Reconstructed seawater pH vs. relative calcification rate (in arbitrary units). (d) Reconstructed seawater pCO₂ (in μ atm) vs. SEM grey scale, which reflects skeletal macro density/porosity (high values = higher density). (e) Reconstructed seawater pCO₂ vs. the rate of linear extension (in μ m/yr). (f) Reconstructed seawater pCO₂ (in μ atm) vs. relative calcification rate (in arbitrary units). 95% confidence error bars are shown for all data. The black lines are ordinary least squares best fit lines through all the data and relevant regression statistics are shown in each panel. The thick grey lines show a cross plotting of Lowess smoothed lines through each timeseries and pick out the long-term relationships between the variables free from the seasonal cycle (shown in Fig. 8).

ocean acidification freeing up *B. soriferum* from carbon limitation. However, given the nature of the CA calcification when subjected to extreme ocean acidification, it is likely that this benefit will be short lived. Indeed, as Ragazzola et al. (2012) have shown, any decrease in skeletal density is already likely to have decreased the strength of the *B. soriferum* skeleton, and hence anthropogenic climate change has already negatively impacted the fitness of this important ecosystem engineer in Loch Sween.

4. Conclusions

In this study we add to the growing body of work demonstrating that the skeletons of coralline algae can act as high-resolution archives of past climate. Here we present a novel methodology based on elemental and isotopic micro-analysis and correlative multimodal imaging that is well suited to exploit the varying chemical and isotopic composition of a CA skeleton to provide seasonal-scale reconstructions of seawater pH. We show there are strong correlations between geochemical tracers and that image segmentation is a useful approach to isolate the central growth axis and avoid areas that have experienced additional stages of calcification. By generating an age model, based on the measured Mg/Ca and nearby temperature logger data, we are able to show that there are marked seasonal variations in pHcf which are strongly negatively correlated with water temperature, in an analogous fashion to pH_{cf} in corals (e.g. Ross et al., 2018). Although the exact cause of this behaviour in CA requires a better understanding of the relevant calcification mechanics, by removing this temperature dependency (as in D'Olivo et al., 2019) and making a pH_{cf}-pH_{sw} calibration using a year of logger data, we reconstruct the temporal evolution of pH_{sw} for Loch Sween at a seasonal scale. The rate of ocean acidification revealed since 2004 (-0.025/year) is over 10x higher than the rates in the open North Atlantic (Ma et al., 2023), but is very similar to that recorded by the

Stonehaven Monitoring station off the east coast of Scotland (Findlay et al., 2022). As the water in Loch Sween has become more acidic, the skeleton of *B. soriferm* CS9 became less dense, but the rate of extension and rate of calcification increased. Our reconstructions indicate pCO_{2sw} was low in Loch Sween in the early part of our record (~200 μ atm), but increased from 2004 by on average ~22 μ atm per year to reach around 400 μ atm in 2017 with warm season peaks up to 600 μ atm. The point when Loch Sween switched from being a perennial sink of CO₂ to a seasonal source of CO₂ was around 2008, therefore we propose that as the water of the loch rapidly acidified it gradually freed *B. soriferum* from carbon limitation promoting its growth. However, given the available laboratory and field studies, these benefits may be short lived (Cornwall et al., 2022).

CRediT authorship contribution statement

Ellen MacDonald: Writing – original draft, Investigation. Gavin L. Foster: Writing – review & editing, Writing – original draft, Visualization, Supervision, Project administration, Methodology, Investigation, Funding acquisition, Formal analysis, Conceptualization. Christopher D. Standish: Writing – review & editing, Validation, Methodology, Formal analysis, Data curation. Jacob Trend: Visualization, Methodology. Tessa M. Page: Writing – review & editing. Nicholas A. Kamenos: Supervision, Project administration, Methodology, Investigation, Funding acquisition, Conceptualization.

Declaration of competing interest

The authors declare that they have no known competing financial interests or personal relationships that could have appeared to influence the work reported in this paper.

Data availability

All data used in this study is available as supplementary tables with this publication.

Acknowledgements

Dan Doran & Matthew Beverley-Smith are thanked for their help with sample preparation. Richard Pearce is acknowledged for his help with the scanning electron microscopy and Andy Milton for his invaluable analytical support. This work was funded by NERC UKOA grant to Kamenos and Foster (NE/H017356/1 & NE/H017356/1), a NERC PhD studentship to McDonald (NE/L002590/1), and a Leverhulme grant and ERC Advanced Microns2Reefs (884650) to Foster that supported Standish, Trend and Page.

Supplementary materials

Supplementary material associated with this article can be found, in the online version, at doi:10.1016/j.epsl.2024.118976.

References

- Adey, W.H., 1965. The genus Clathromorphum (Corallinaceae) in the Gulf of Maine. Hydrobiologia 26, 539–573.
- Anagnostou, E., Williams, B., Westfield, I., Foster, G.L., Ries, J.B., 2019. Calibration of the pH-811B and temperature-Mg/Li proxies in the long-lived high-latitude crustose coralline red alga Clathromorphum compactum via controlled laboratory experiments. Geochim. Cosmochim. Acta 254, 142–155.
- Aonishi, T., Hirata, T., Kuwatani, T., Fujimoto, M., Chang, Q., Kimura, J.-I., 2018. A numerical inversion method for improving the spatial resolution of elemental imaging by laser ablation-inductively coupled plasma-mass spectrometry. J. Anal. At. Spectrom. 33, 2210–2218.
- Attard, K.M., Stahl, H., Kamenos, N.A., Turner, G., Burdett, H.L., Glud, R.N., 2015. Benthic oxygen exchange in a live coralline algal bed and an adjacent sandy habitat: an eddy covariance study. Mar. Ecol. Prog. Ser. 535, 99–115.
- Bates, N.R., Astor, Y.M., Church, M.J., Currie, K., Dore, J.E., Gonzalez-Davila, M., Lorenzoni, L., Muller-Karger, F., Olafsson, J., Santana-Casiano, J.M., 2014. A time series view of changing ocean chemistry due to coean uptake of anthropogenic CO₂ and ocean acidification. Oceanography 27, 126–141.
- Bergstrom, E., Ordoñez, A., Ho, M., Hurd, C., Fry, B., Diaz-Pulido, G., 2020. Inorganic carbon uptake strategies in coralline algae: plasticity across evolutionary lineages under ocean acidification and warming. Mar. Environ. Res. 161, 105107.
- Brodie, J., Williamson, C.J., Smale, D.A., Kamenos, N.A., Mieszkowska, N., Santos, R., Cunliffe, M., Steinke, M., Yesson, C., Anderson, K.M., Asnaghi, V., Brownlee, C., Burdett, H.L., Burrows, M.T., Collins, S., Donohue, P.J.C., Harvey, B., Foggo, A., Noisette, F., Nunes, J., Ragazzola, F., Raven, J.A., Schmidt, D.N., Suggett, D., Teichberg, M., Hall-Spencer, J.M., 2014. The future of the northeast Atlantic benthic flora in a high CO₂ world. Ecol. Evol. 4, 2787–2798.
- Burton, E.A., Walter, L.M., 1987. Relative precipitation rates of aragonite and Mg calcite from seawater: temperature or carbonate ion control? Geology 15, 111–114.
- Carstensen, J., Duarte, C.M., 2019. Drivers of pH variability in coastal ecosystems. Environ. Sci. Technol. 53, 4020–4029.
- Catanzaro, E.J., Champion, C.E., Garner, E.L., Marinenko, G., Sappenfield, K.M., Shields, W.R., 1970. Boric Assay; Isotopic, and Assay Standard Reference Materials.
- Chalk, T.B., Standish, C.D., D'Angelo, C., Castillo, K.D., Milton, J.A., Foster, G.L., 2021.
 Mapping coral calcification strategies from in situ boron isotope and trace element measurements of the tropical coral Siderastrea siderea. Sci. Rep. 11, 472.
- Cornwall, C.E., Comeau, S., McCulloch, M.T., 2017. Coralline algae elevate pH at the site of calcification under ocean acidification. Glob. Chang. Biol. 23, 4245–4256.
- Cornwall, C.E., Harvey, B.P., Comeau, S., Cornwall, D.L., Hall-Spencer, J.M., Peña, V., Wada, S., Porzio, L., 2022. Understanding coralline algal responses to ocean acidification: meta-analysis and synthesis. Glob. Chang. Biol. 28, 362–374.
- D'Olivo, J.P., Ellwood, G., DeCarlo, T.M., McCulloch, M.T., 2019. Deconvolving the long-term impacts of ocean acidification and warming on coral biomineralisation. Earth Planet. Sci. Lett. 526, 115785.
- Dickson, A.G., 1990. Thermodynamics of the dissociation of boric acid in synthetic seawater from 273.15 to 318.15 K. Deep Sea Research Part A. Oceanograph. Res. Pap. 37, 755–766.
- Donald, H.K., Ries, J.B., Stewart, J.A., Fowell, S.E., Foster, G.L., 2017. Boron isotope sensitivity to seawater pH change in a species of Neogoniolithon coralline red alga. Geochim. Cosmochim. Acta 217, 240–253.
- Duarte, C.M., Hendriks, I.E., Moore, T.S., Olsen, Y.S., Steckbauer, A., Ramajo, L., Carstensen, J., Trotter, J.A., McCulloch, M., 2013. Is ocean acidification an openocean syndrome? Understanding anthropogenic impacts on seawater pH. Estuar. Coast. 36. 221–236.
- Eagle, R.A., Guillermic, M., De Corte, I., Alvarez Caraveo, B., Bove, C.B., Misra, S., Cameron, L.P., Castillo, K.D., Ries, J.B., 2022. Physicochemical control of Caribbean

- Coral Calcification linked to host and symbiont responses to varying pCO_2 and temperature. J. Mar. Sci. Eng. 10, 1075.
- Evans, D., Gerdes, A., Coenen, D., Marschall, H.R., Müller, W., 2021. Accurate correction for the matrix interference on laser ablation MC-ICPMS boron isotope measurements in CaCO₃ and silicate matrices. J. Anal. At. Spectrom. 36, 1607–1617.
- Eyre, B.D., Cyronak, T., Drupp, P., De Carlo, E.H., Sachs, J.P., Andersson, A.J., 2018. Coral reefs will transition to net dissolving before end of century. Science 359, 908–911.
- Farmer, J.R., Branson, O., Uchikawa, J., Penman, D.E., Hönisch, B., Zeebe, R.E., 2019. Boric acid and borate incorporation in inorganic calcite inferred from B/Ca, boron isotopes and surface kinetic modeling. Geochim. Cosmochim. Acta 244, 229–247.
- Ferrari, M.C.O., Manassa, R.P., Dixson, D.L., Munday, P.L., McCormick, M.I., Meekan, M. G., Sih, A., Chivers, D.P., 2012. Effects of ocean acidification on learning in coral reef fishes. PLoS ONE 7, e31478.
- Fietzke, J., Ragazzola, F., Halfar, J., Dietze, H., Foster, L.C., Hansteen, T.H., Eisenhauer, A., Steneck, R.S., 2015. Century-scale trends and seasonality in pH and temperature for shallow zones of the Bering Sea. Proceed. Natl. Acad. Sci. 112, 2960–2965.
- Findlay, H.S., Artoli, Y., Birchenough, S.N.R., Hartman, S., Leon, P., Stiasny, M., 2022. Ocean acidification around the UK and Ireland. MCCIP Sci. Rev. 2022.
- Fitzer, S.C., Phoenix, V.R., Cusack, M., Kamenos, N.A., 2014. Ocean acidification impacts mussel control on biomineralisation. Sci. Rep. 4, 6218.
- Foster, G.L., Pogge von Strandmann, P.A.E., Rae, J.W.B., 2010. Boron and magnesium isotopic composition of seawater. Geochem. Geophys. Geosyst. 11, Q08015, 08010.01029/02010GC003201.
- Fox, M., Tripathy-Lang, A., Shuster, D.L., 2017. Improved spatial resolution of elemental maps through inversion of LA-ICP-MS data. Chem. Geol. 467, 30–41.
- Gabrielson, P.W., Maneveldt, G.W., Hughey, J.R., Peña, V., 2023. Taxonomic contributions to Hapalidiales (Corallinophycidae, Rhodophyta): Boreolithothamnion gen. nov., Lithothamnion redefined and with three new species and Roseolithon with new combinations. J. Phycol. 59, 751–774.
- Gagnon, A.C., Gothmann, A.M., Branson, O., Rae, J.W.B., Stewart, J.A., 2021. Controls on boron isotopes in a cold-water coral and the cost of resilience to ocean acidification. Earth Planet. Sci. Lett. 554, 116662.
- Gattuso, J.-P., Epitalon, J.-M., Lavigne, H., Orr, J.C., 2022. seacarb: Seawater Carbonate Chemistry. R package version 3.3.1.
- Gattuso, J.-P., Magnan, A., Bille, R., Cheung, W.W.L., Howes, E.L., Joos, F., Allemand, D., Bopp, L., Cooley, S.R., Eakin, C.M., Hoegh-Guldberg, O., Kelly, R.P., Portner, H.-O., Rodgers, A.D., Baxter, J.M., Laffoley, D., Osborn, D., Rankovic, A., Rochette, J., Sumaila, U.R., Treyer, S., Turley, C., 2015. Contrasting futures for ocean and society from different anthropogenic CO2 emission scenarios. Science 349 aac4722-4721 aac4722-4710.
- Gilbert, P., Bergmann, K.D., Boekelheide, N., Tambutté, S., Mass, T., Marin, F., Adkins, J. F., Erez, J., Gilbert, B., Knutson, V., Cantine, M., Hernández, J.O., Knoll, A.H., 2022. Biomineralization: integrating mechanism and evolutionary history. Sci. Adv. 8, eabl9653.
- Guo, W., 2019. Seawater temperature and buffering capacity modulate coral calcifying pH. Sci. Rep. 9, 1189.
- Gutjahr, M., Bordier, L., Douville, E., Farmer, J., Foster, G.L., Hathorne, E.C., Hönisch, B., Lemarchand, D., Louvat, P., McCulloch, M., Noireaux, J., Pallavicini, N., Rae, J.W.B., Rodushkin, I., Roux, P., Stewart, J.A., Thil, F., You, C.-F., 2021. Sub-permil interlaboratory consistency for solution-based boron isotope analyses on marine carbonates. Geostand. Geoanalyt. Res. 45. 59–75.
- carbonates. Geostand. Geoanalyt. Res. 45, 59–75.
 Halfar, J., Zack, T., Kronz, A., Zachos, J.C., 2000. Growth and high-resolution paleoenvironmental signals of rhodoliths (coralline red algae): a new biogenic archive. J. Geophys. Res. Ocean. 105, 22107–22116.
- Hemming, N.G., Hanson, G.N., 1992. Boron isotopic composition and concentration in modern marine carbonates. Geochim. Cosmochim. Acta 56, 537–543.
- Henehan, M.J., Foster, G.L., Bostock, H.C., Greenop, R., Marshall, B., Wilson, P.A., 2016.
 A new boron isotope-pH calibration for Orbulina universa, with implications for understanding and accounting for vital effects. Earth Planet. Sci. Lett. 454, 282–292.
- Secretariat of the Convention on Biological Diversity, 2014. An Updated Synthesis of the Impacts of Ocean Acidification on Marine Biodiversity (Eds: S. Hennige, J.M. Roberts & P. Williamson). Technical Series No. 75, Montreal, p. 99.
- Hijmans, R., 2022. Raster: Geographic Data Analysis and Modeling. R package version 3.5-21.
- Holcomb, M., Venn, A.A., Tambutte, E., Allemand, D., Trotter, J., McCulloch, M.T., 2014. Coral calcifying fluid pH dictates response to ocean acidification. Sci. Rep. 4, 1–4.
- Hönisch, B., Hemming, S., Grottoli, A.G., Amat, A., Hanson, G.N., Bijma, J., 2004. Assessing scleractinian corals as recorders for paleo-pH: empirical calibration and vital effects. Geochim. Cosmochim. Acta 68, 3675–3685.
- Hurd, C.L., Cornwall, C.E., Currie, K., Hepburn, C.D., McGraw, C.M., Hunter, K.A., Boyd, P.W., 2011. Metabolically induced pH fluctuations by some coastal calcifiers exceed projected 22nd century ocean acidification: a mechanism for differential susceptibility? Glob. Chang. Biol. 17, 3254–3262.
- Inoue, M., Nohara, M., Okai, T., Suzuki, A., Kawahata, H., 2004. Concentrations of trace elements in carbonate reference materials coral JCp-1 and giant clam JCt-1 by inductively coupled plasma-mass spectrometry. Geostandard. Geoanalyti. Res. 28, 411-416.
- Irvine, L.M., Chamberlain, Y.M., 1994. Seaweeds of the British Isles. Volume 1. Rhodophyta. Part 2B Corallinales, Hildenbrandiales. J. Marine Biolog. Assoc. U.K. 74, 986-986.
- Jochum, K.P., Weis, U., Stoll, B., Kuzmin, D., Yang, Q., Raczek, I., Jacob, D.E., Stracke, A., Birbaum, K., Frick, D.A., Günther, D., Enzweiler, J., 2011. Determination of reference values for NIST SRM 610–617 glasses following ISO guidelines. Geostand. Geoanalyt. Res. 35, 397–429.

- Kamenos, N.A., Burdett, H.L., Aloisio, E., Findlay, H.S., Martin, S., Longbone, C., Dunn, J., Widdicombe, S., Calosi, P., 2013. Coralline algal structure is more sensitive to rate, rather than the magnitude, of ocean acidification. Glob. Change Biol. 19, 3621–3628.
- Kamenos, N.A., Cusack, M., Moore, P.G., 2008. Coralline algae are global palaeothermometers with bi-weekly resolution. Geochim. Cosmochim. Acta 72, 771–779.
- Kamenos, N.A., Hoey, T.B., Nienow, P., Fallick, A.E., Claverie, T., 2012. Reconstructing Greenland ice sheet runoff using coralline algae. Geology 40, 1095–1098.
- Kamenos, N.A., Law, A., 2010. Temperature controls on coralline algal skeletal growth. J. Phycol. 46, 331–335.
- Karreman, M.A., Mercier, L., Schieber, N.L., Solecki, G., Allio, G., Winkler, F., Ruthensteiner, B., Goetz, J.G., Schwab, Y., 2016. Fast and precise targeting of single tumor cells in vivo by multimodal correlative microscopy. J. Cell. Sci. 129, 444–456.
- Klochko, K., Kaufman, A.J., Yoa, W., Byrne, R.H., Tossell, J.A., 2006. Experimental measurement of boron isotope fractionation in seawater. Earth Planet. Sci. Lett. 248, 261–270
- Krief, S., Hendy, E.J., Fine, M., Yam, R., Meibom, A., Foster, G.L., Shemesh, A., 2010. Physiological and isotopic responses of scleractinian corals to ocean acidification. Geochm. Cosmochim. Acta 74, 4988–5001.
- Lee, K., Kim, T.-W., Byrne, R.H., Millero, F.J., Feely, R.A., Liu, Y.-M., 2010. The universal ratio of boron to chlorinity for the North Pacific and North Atlantic oceans. Geochim. Cosmochim. Acta 74, 1801–1811.
- Lough, J.M., Cantin, N.E., Benthuysen, J.A., Cooper, T.F., 2016. Environmental drivers of growth in massive Porites corals over 16 degrees of latitude along Australia's northwest shelf. Limnol. Oceanogr. 61, 684–700.
- Ma, D., Gregor, L., Gruber, N., 2023. Four decades of trends and drivers of global surface ocean acidification. Glob. Biogeochem. Cycl. 37, e2023GB007765.
- MacDonald, E., Byrne, M., Deaker, D.J., Foster, G.L., Garbarda, S.T., MacDonald, J., Rae, J.W.B., Slaymark, C., Kamenos, N.A., n.d. in review. Timing of calcification and environmental variability determine pH proxy fidelity in coastal calcifying macroalgae. Limnol. Oceanogr.
- Mao, J., 2019. The Role of Red Coralline Algal Habitats as Blue Carbon Stores. School of Geographical and Earth Sciences. University of Glasgow
- Mao, J., Burdett, H.L., Kamenos, N.A., 2024. Efficient carbon recycling between calcification and photosynthesis in red coralline algae. Biol. Lett. 20, 20230598.
- McCoy, S.J., Pueschel, C.M., Cornwall, C.E., Comeau, S., Kranz, S.A., Spindel, N.B., Borowitzka, M.A., 2023. Calcification in the coralline red algae: a synthesis. Phycologia 62, 648–666.
- Meyers, S.R., 2014. Astrochron: an R Package for Astrochronology.
- Nash, M.C., Diaz-Pulido, G., Harvey, A.S., Adey, W., 2019. Coralline algal calcification: a morphological and process-based understanding. PLoS ONE 14, e0221396.
- Ostle, C., Williamson, P., Artioli, Y., Bakker, D.C.E., Birchenough, S., Davis, C.E., Dye, S., Edwards, M., Findlay, H.S., Greenwood, N., Hartman, S., Humphreys, M.P., Jickells, T., Johnson, M., Landschützer, P., Parker, R., Pearce, D., Pinnegar, J., Robinson, C., Schuster, U., Silburn, B., Thomas, R., Wakelin, S., Walsham, P., Watson, A.J., 2016. Carbon Dioxide and Ocean Acidification Observations in UK Waters: Synthesis Report with a Focus on 2010-2015, p. 42.
- Peltzer, E.T., 1998. Matlab Scripts for Oceanographic Calculations.
- Peña, V., Bélanger, D., Gagnon, P., Richards, J.L., Le Gall, L., Hughey, J.R., Saunders, G. W., Lindstrom, S.C., Rinde, E., Husa, V., Christie, H., Fredriksen, S., Hall-Spencer, J. M., Steneck, R.S., Schoenrock, K.M., Gitmark, J., Grefsrud, E.S., Anglès d'Auriac, M. B., Legrand, E., Grall, J., Mumford, T.F., Kamenos, N.A., Gabrielson, P.W., 2021. Lithothamnion (Hapalidiales, Rhodophyta) in the changing Arctic and Subarctic: DNA sequencing of type and recent specimens provides a systematics foundation. Eur. J. Phycol. 56, 468–493.

- Rae, J.W.B., Burke, A., Robinson, L.F., Adkins, J.F., Chen, T., Cole, C., Greenop, R., Li, T., Littley, E.F.M., Nita, D.C., Stewart, J.A., Taylor, B.J., 2018. CO2 storage and release in the deep Southern Ocean on millennial to centennial timescales. Nature 562, 569–573
- Rae, J.W.B., Foster, G.L., Schmidt, D.N., Elliott, T., 2011. Boron isotopes and B/Ca in benthic foraminifera: proxies for the deep ocean carbonate system. Earth Planet. Sci. Lett. 302, 403–413.
- Ragazzola, F., Foster, L.C., Form, A., Anderson, P.S.L., Hansteen, T.H., Fietzke, J., 2012.
 Ocean acidification weakens the structural integrity of coralline algae. Glob. Chang.
 Biol. 18, 2804–2812.
- Standish, C.D., Chalk, T.B., Babila, T.L., Milton, J.A., Palmer, M.R., Foster, G.L., 2019. The effect of matrix interferences on in situ boron isotope analysis by laser ablation multi-collector inductively coupled plasma mass spectrometry. Rapid Commun. Mass Spectrom. 33, 959–968.
- Standish, C.D., Trend, J., Kleboe, J., Chalk, T.B., Mahajan, S., Milton, J.A., Page, T.M., Robinson, L.F., Stewart, J.A., Foster, G.L., 2024. Correlative geochemical imaging of Desmophyllum dianthus reveals biomineralisation strategy as a key coral vital effect. Sci. Rep. 14, 11121.
- Stewart, J.A., Anagnostou, E., Foster, G.L., 2016. An improved boron isotope pH proxy calibration for the deep-sea coral Desmophyllum dianthus through sub-sampling of fibrous aragonite. Chem. Geol. 447, 148–160.
- Sutton, A.J., Feely, R.A., Maenner-Jones, S., Musielwicz, S., Osborne, J., Dietrich, C., Monacci, N., Cross, J., Bott, R., Kozyr, A., Andersson, A.J., Bates, N.R., Cai, W.J., Cronin, M.F., De Carlo, E.H., Hales, B., Howden, S.D., Lee, C.M., Manzello, D.P., McPhaden, M.J., Meléndez, M., Mickett, J.B., Newton, J.A., Noakes, S.E., Noh, J.H., Olafsdottir, S.R., Salisbury, J.E., Send, U., Trull, T.W., Vandemark, D.C., Weller, R. A., 2019. Autonomous seawater pCO₂ and pH time series from 40 surface buoys and the emergence of anthropogenic trends. Earth Syst. Sci. Data 11, 421–439.
- van der Heijden, L.H., Kamenos, N.A., 2015. Reviews and syntheses: calculating the global contribution of coralline algae to total carbon burial. Biogeosciences 12, 6429–6441.
- Walter, A., Paul-Gilloteaux, P., Plochberger, B., Sefc, L., Verkade, P., Mannheim, J.G., Slezak, P., Unterhuber, A., Marchetti-Deschmann, M., Ogris, M., Bühler, K., Fixler, D., Geyer, S.H., Weninger, W.J., Glösmann, M., Handschuh, S., Wanek, T., 2020. Correlated multimodal imaging in life sciences: expanding the biomedical horizon. Front. Phys. 8.
- White, M.M., Mulineaux, L.S., McCorkle, D.C., Cohen, A.L., 2014. Elevated pCO₂ exposure during fertilization of the bay scallop Argopecten irradians reduces larval survival but not subsequent shell size. Mar. Ecol. Prog. Ser. 498, 173–186.
- Williams, B., Chan, P.T.W., Westfield, I.T., Rasher, D.B., Ries, J., 2021. Ocean acidification reduces skeletal density of hardground-forming high-latitude crustose coralline algae. Geophys. Res. Lett. 48, e2020GL091499.
- Worrall, F., Jarvie, H.P., Howden, N.J.K., Burt, T.P., 2016. The fluvial flux of total reactive and total phosphorus from the UK in the context of a national phosphorus budget: comparing UK river fluxes with phosphorus trade imports and exports. Biogeochemistry 130, 31–51.
- Yudelman, E.A., Slowey, N.C., 2022. Coral extension rate analysis using computed axial tomography. Coral Reefs 41, 973–985.
- Zeebe, R., Wolf-Gladrow, D.A., 2001. CO₂ in Seawater: Equilibrium, Kinectics, Isotopes. Elsevier, Amesterdam.
- Zeileis, A., Grothendieck, G., 2005. zoo: S3 infrastructure for regular and irregular time series. J. Stat. Softw. 14, 1–27.
- Zopf, L.M., Heimel, P., Geyer, S.H., Kavirayani, A., Reier, S., Fröhlich, V., Stiglbauer-Tscholakoff, A., Chen, Z., Nics, L., Zinnanti, J., Drexler, W., Mitterhauser, M., Helbich, T., Weninger, W.J., Slezak, P., Obenauf, A., Bühler, K., Walter, A., 2021. Cross-modality imaging of murine tumor vasculature—a feasibility study. Molecul. Imag. Biol. 23, 874–893.